Color-PTV measurement and CFD-DEM simulation of the dynamics of poly-disperse particle systems in a pseudo-2D fluidized bed

Zhaochen Jiang [a,*], Thomas Hagemeier [b], Andreas Bück [a,c], Evangelos Tsotsas [a]

[a] NaWiTec, Thermal Process Engineering, Otto-von-Guericke University Magdeburg, Universitaetsplatz 2, 39106 Magdeburg, Germany
[b] The Laboratory of Fluid Dynamics and Technical Flows, Otto-von-Guericke University Magdeburg, Universitaetsplatz 2, 39106 Magdeburg, Germany
[c] Institute of Particle Technology (LFG), FAU Erlangen-Nuremberg, Cauerstr. 4, 91058 Erlangen, Germany

HIGHLIGHTS

- Novel color-PTV is introduced to measure individual particle velocities in mixtures.
- Comprehensive verification of color-PTV method is conducted by CFD-DEM data.
- Detailed comparisons are conducted between CFD-DEM and color-PTV measurements.
- Correction for effect of particle size dispersity is required for accurate CFD-DEM.

GRAPHICAL ABSTRACT
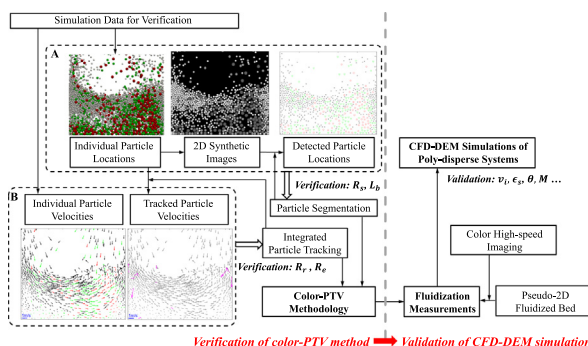
ARTICLE INFO

ABSTRACT

In a pseudo-2D fluidized bed, a new color particle tracking velocimetry (PTV) method, integrating the Voronoi tracking algorithm and the relaxation probability tracking algorithm, is proposed to measure velocities of individual particles with different sizes marked by distinguishable colors. Thorough verification of the color-PTV methodology is conducted based on synthetic images generated from CFD-DEM simulation data, in terms of segmentation bias, segmentation ratio, recovery ratio and error ratio. The novel color-PTV methodology shows very good performance in simultaneously tracking a large number of different individual particles in poly-disperse systems. Experimental results are used to compare with CFD-DEM simulations using different drag models. Simulations with correction for the effect of particle size dispersity in the drag model show significantly better agreement with respect to the mixing index, time-averaged volumetric particle flux, distributions of individual particle velocity as well as distributions of particle granular temperature.

© 2018 Elsevier Ltd. All rights reserved.

1. Introduction

Fluidized bed spray granulation, coating and agglomeration are widely used in chemical and pharmaceutical industries to produce food, pharmaceuticals, fertilizers, powder catalysts and cosmetics, as a result of excellent heat and mass transfer between solid particles and fluid phase (Mörl et al., 2007; Tsotsas and Mujumdar, 2011). Since the wet granulation process is highly complex, it is often operated inefficiently in industrial applications. The enhanced understanding of underlying multi-scale particle dynamics is required to improve the efficiency of processes and to achieve high product quality (Tsotsas, 2012, 2015).

* Corresponding author.
E-mail address: zhaochen.jiang@ovgu.de (Z. Jiang).

Nomenclature

c	volume fraction of the smallest particles in each sample [–]
d_p	particle diameter [mm]
d_{32}	Sauter mean diameter [mm]
e	coefficient of restitution [–]
E	Young's modulus [Pa]
F	normalized drag force [–]
$\boldsymbol{f}_{pf}$	particle-fluid interaction force (particle level, vector) [N]
$\boldsymbol{f}_c$	particle-particle interaction force (vector) [N]
$\boldsymbol{f}_d$	drag force (vector) [N]
F_p	correction factor for poly-disperse effect [–]
$\boldsymbol{F}_{pf}$	particle-fluid interaction force (cell level, vector) [N]
$\boldsymbol{g}$	acceleration due to gravity (vector) [m/s^2]
$I, \bar{I}$	intensity and mean intensity in the matrix of raw image [–]
I_m	moment of inertia [kg · m^2]
L_b	bias of the segmentation location [pixel]
k	stiffness coefficient [–]
k_r	rolling coefficient [–]
m	mass of particle [kg]
N_1	number of particles in a CFD cell [–]
N_2	number of particles in interaction with i [–]
N_e	equivalent number of particles in each sample [–]
N_s	number of samples [–]
p	pressure [Pa]
P_s	global volume fraction of the smallest particles in a mixture [–]
R	particle radius [m]
R_e	error ratio [–]
R_r	recovery ratio [–]
R_s	segmentation ratio [–]
Re_p	Reynolds number of particle [–]
$s, \bar{s}$	intensity and mean intensity in the matrix of template particle [–]
S_f	scale factor [pixel/mm]
S^2	actual variance of particle volume fraction of the smallest particles [–]
$t, \Delta t$	time, time step size [s]
T_t	tangential torque (vector) [N · s]
T_r	rolling torque (vector) [N · s]
$\boldsymbol{v}_p$	particle velocity (vector) [m/s]
$v_{c,max}$	maximum collision velocity [m/s]
U_{mf}	minimum fluidization velocity [m/s]
U_g	superficial gas velocity [m/s]
V	volume [m^3]

x, y, z	Cartesian coordinates [m]
y_i	diameter ratio [–]

Greek symbols

α	damping ratio [–]
β_{pf}	momentum exchange coefficient [kg/(m^3 · s)]
γ	normalized cross-correlation coefficient [–]
ϵ	volume fraction [–]
η	damping coefficient [–]
Θ	particle granular temperature [m^2/s^2]
μ_g	gas dynamic viscosity [Pa · s]
μ_{fc}	friction coefficient [–]
ρ	density [kg/m^3]
σ	Poisson's ratio [Pa · s]
τ_H	Hertzian collision time [s]
τ_f	fluid stress tensor [Pa]
$\boldsymbol{\omega}$	particle angular velocity (vector) [rad/s]

Subscripts

$1, 2$	different particle classes, or time steps
$2D$	two-dimensional space
eq	equivalent
f	fluid
i, j, k	indices
n	normal direction
p	particle
t	tangential direction

Abbreviations

CFD	computational fluid dynamics
CoR	coefficient of restitution
DEM	discrete element method
DIA	digital image analysis
FOV	field of view
HSV	hue-saturation-value color space
MPT	magnetic particle tracking
MRI	magnetic resonance imaging
PEPT	positron emission particle tracking
PIV	particle imaging velocimetry
PTV	particle tracking velocimetry
PBM	population balance modeling
RGB	red-green-blue color space
SD	standard deviation

A strong emphasis has been placed on experimental studies of particle behavior in mono-disperse fluidized beds, including particle image velocimetry (PIV) combined with digital image analysis (DIA), particle tracking velocimetry (PTV), positron emission particle tracking (PEPT), magnetic particle tracking (MPT), and magnetic resonance imaging (MRI) (Link et al., 2008; Holland et al., 2008; Mohs et al., 2009; van Buijtenen et al., 2011; de Jong et al., 2012; Hagemeier et al., 2015a,b; Jiang et al., 2017b). Depending on different objectives of investigations, the measured variables associated with particle dynamics (the motion of solid phase) were the particle velocity, the granular temperature, the particle cycle time and residence time; and particle collision dynamics. The motion of particles in a fluidized bed is very complex due to movement of bubbles and random particle-particle or particle-wall interactions. Therefore, a reliable and accurate tracking algorithm is required to simultaneously track a large number of particles in such complex granular flow (Hagemeier et al., 2015b; Jiang et al., 2017b). Moreover, the PTV technique for the mono-disperse system can

be readily extended to poly-disperse systems of particles with different sizes marked by distinguishable colors. However, the PTV technique is limited to visualized experimental configurations.

Indeed, poly-disperse systems (with particles of different sizes, different densities, or both different sizes and densities) are commonly encountered in practical applications. As an important phenomenon in poly-disperse fluidization, the segregation of particles strongly influences particle formation processes; for instance, it is essential to guarantee that smaller drug particles can be uniformly blended into larger granules in fluidized bed granulation (Muzzio et al., 2002). Due to their industrial importance, the segregation and the mixing behavior have been experimentally studied using various techniques, such as digital image analysis (DIA) (Goldschmidt et al., 2003a; Olaofe et al., 2013), and frozen bed sieving (Lu et al., 2003; Joseph et al., 2007). On the one hand, the segregation state was determined by several competing factors associated with particle dynamics and hydrodynamics, including drag force, turbulence of gas-phase, particle granular temperature

and particle collisions (Joseph et al., 2007). On the other hand, particle dynamics and hydrodynamics were strongly affected by the size-ratio and the density-ratio of different particles. However, published experimental studies of particle dynamics in poly-disperse systems are very limited due to inherent difficulties in measurement, especially tracking individual particles with different sizes in fluidized beds.

In the last decade, the computational fluid dynamics-discrete element method (CFD-DEM) has been extensively applied in simulations of complex granular flow. The methodology and comprehensive numerical algorithms of CFD-DEM have been systematically discussed in the reviews of Zhu et al. (2007), Deen et al. (2007) and Zhou et al. (2010). The CFD-DEM approach can capture the majority of macro-scale and micro-scale characteristics of multi-phase flow, simultaneously providing an insight into underlying physics at particle-scale. Moreover, some aspects that are difficult to be captured in the traditional continuum description of the solid phase by the two-fluid method closed by the kinetic theory of granular flow (Deen et al., 2007; Gidaspow, 1994), such as poly-dispersity, cohesion and non-spherical particles, can be readily incorporated in DEM. With the help of the CFD-DEM approach, the segregation and the mixing behavior in fluidized beds, characterized by the mixing index that indicates the overall segregation state of mixture (Goldschmidt et al., 2003a; Lacey, 1954), have been numerically studied and compared with measurements (Bokkers et al., 2004; Feng et al., 2004; Beetstra et al., 2007a; Olaofe et al., 2014). It was found that the drag model for poly-disperse systems is important for the accuracy of predictions of the mixing degree. Beetstra et al. (2007a) proposed a correction factor, integrated diameter ratio and porosity, based on lattice-Boltzmann simulations, which gives a significant improvement over drag models for mono-disperse systems. Notably, the comparison of mixing index is not enough for the comprehensive validation of CFD-DEM simulations of poly-disperse systems, since particle dynamics are not directly included in the mixing index.

As a well established macroscopic approach to predict particle formation processes, the population balance modeling (PBM) has been widely used in investigations at industrial scale (Ramkrishna, 2000; Immanuel and Doyle, 2005; Bück et al., 2015). When microscopic particle dynamics from CFD-DEM simulations are further integrated with the population balance modeling, a multi-scale model can be created to predict wet particle granulation processes, leading to a better understanding of the effects of process parameters and particle properties on critical quality attributes (Goldschmidt et al., 2003b; Freireich et al., 2011; Barrasso and Ramachandran, 2015). The performance of the multi-scale coupling approach depends on the accuracy of CFD-DEM simulations of poly-disperse particle systems, which have to be validated not only with regard to segregation (or mixing) behavior, but also to detailed particle dynamics.

The objective of this study is to develop a new color-PTV method to study both particle dynamics and mixing behavior of poly-disperse systems in a pseudo-2D fluidized bed. As an indispensable aspect, the verification of particle segmentation algorithm and particle tracking algorithm in the new color-PTV methodology is performed based on CFD-DEM simulation data with exactly the same particles and fluidization conditions. The particle orientated features of the CFD-DEM approach are very suitable to generate synthetic images for verifying the PTV method, focusing on tracking individual particles. In addition, results of color-PTV measurements, including profiles of particle volumetric flux, distributions of particle velocity, distributions of granular temperature and the mixing index, are used as a benchmark to compare with the CFD-DEM simulations.

The structure of this contribution is: Section 2 illustrates the experimental setup, mixture properties and the high-speed imaging system. Section 3 introduces the new color-PTV methodology, including color classification approach, particle segmentation algorithm and integrated particle tracking algorithms. Section 4 systematically explains the verification of color-PTV methodology by CFD-DEM simulation data, on the basis of quantitative criterion. A short description of CFD-DEM simulation is also given in this section. Section 5 presents and discusses the color-PTV measurement results of one binary mixture case and one ternary mixture case. Furthermore, detailed comparisons are performed with CFD-DEM simulations using drag models with or without correction for the effect of particle size dispersity. Section 6 presents conclusions and outlook on further research.

2. Experimental setups

2.1. Pseudo-2D fluidized bed

Fluidization experiments were conducted in a laboratory scale pseudo-2D fluidized bed, as shown schematically in Fig. 1. The dimensions of the process chamber are 100 mm, 340 mm and 14 mm in width, height and depth, respectively. The front and side walls were made of acrylic glass and the back wall was made of aluminum. Pressurized air was used as fluidization gas. Accurate control of inlet gas flow rate was achieved by application of a calibrated mass flow controller. A 3 mm porous plate distributor with a mean pore size of 10 μ m was used to generate the relatively uniform gas distribution.

Three different fractions of γ-alumina particles with diameter d_p of 3.0 mm, 2.5 mm and 1.8 mm (Geldart class D) were used in measurements, and detailed particle properties and operation conditions for two cases are summarized in Table 1. The size and sphericity of particles were measured by Camsizer (Retsch GmbH). The density of particles was measured by a pycnometer (GeoPyc 1360, Micromeritics GmbH). The coefficient of restitution (CoR) of particles was evaluated from collision events that were generated by a vibratory feeder and captured by a high speed imaging system (Jiang et al., 2017). The minimum fluidization velocities U_{mf} of different particles were calculated using the correlation of Wen and Yu (1966). Regarding the initial conditions, different particles are vertically layered with equal volume of 20 cm³ in *Case 1*, and horizontally layered with equal mass of 10.6 g in *Case 2*, as also shown in Fig. 1. The static height in both cases was approximately 28.5 mm. The Sauter mean diameter d_{32} in both cases was approximately 2.15 mm. In each case, the gas flow rate was manually increased from zero to a superficial gas velocity of 2.8 m/s in approximately 1 s. The gas flow velocities experienced fluctuations of 0.02 m/s during the measurements.

2.2. Imaging system

The motion of particles in the poly-disperse particle systems was observed with a high-speed color camera (Phantom Micro-310, CMOS chip, 1280 × 800 pixels). It was operated at full spatial resolution with a frame rate of 1000 fps, an exposure time of 1/8000 s and a dynamic range of 12 bit. The imaging system was controlled by the DaVis image acquisition software (LaVision). The entire bed was illuminated by two continuous 400 W halogen lamps during measurements. An optical lens with 60 mm focal length was employed to achieve suitable size of field of view (FOV). The f-number, relative focal length to effective aperture, was set at the minimum value of 2.8, which yields a minimum depth of focus field and maximum light exposure during high speed imaging. The depth of field was approximately 8 mm in current configuration.
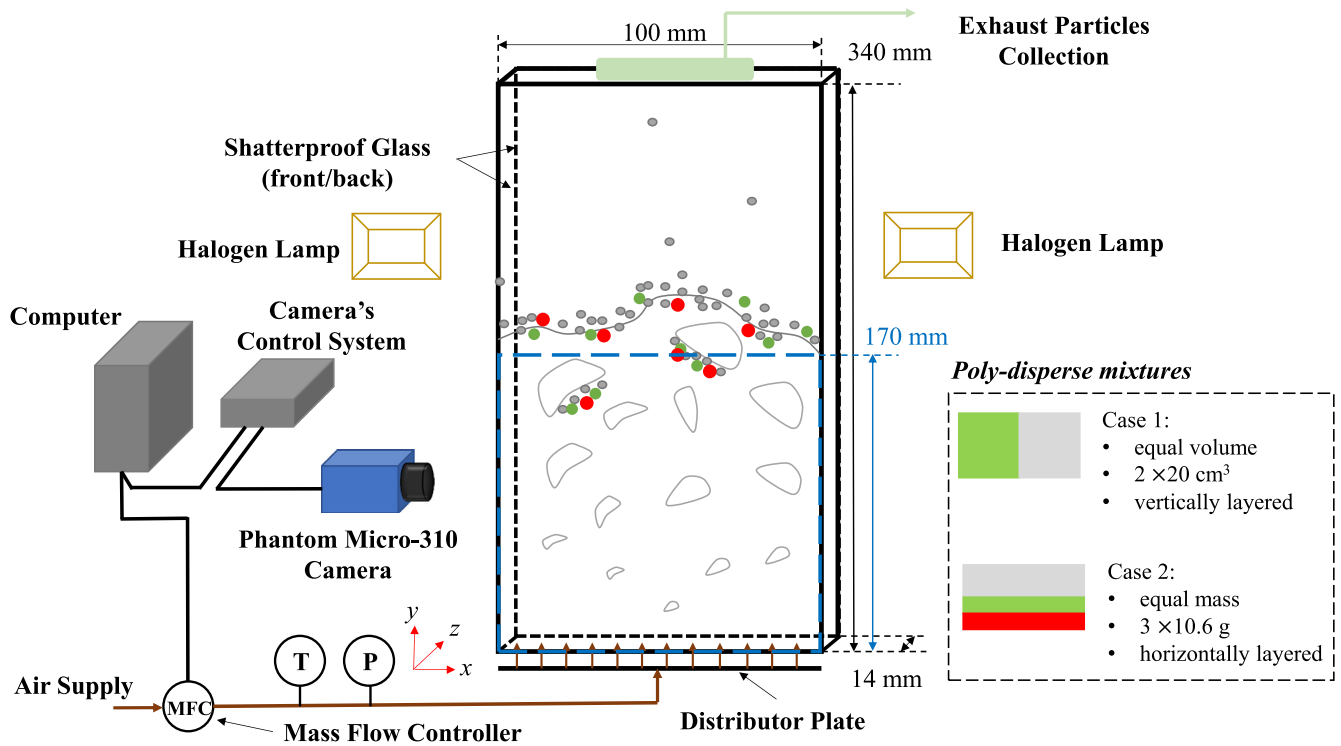
Fig. 1. Sketch of laboratory-scale pseudo-2D fluidized bed configuration with apparatus dimensions and initial mixture characteristics.

Table 1
Particle properties, characteristics of mixtures and operation conditions.

d_p [mm]	ρ_p [kg/m³]	Sphericity [–]	CoR e [–]	U_{mf} [m/s]	Color
Particle properties					
3.0	1478	0.97	0.79	1.05	Red
2.5	1450	0.97	0.81	0.91	Green
1.8	985	0.96	0.81	0.53	White

Case	Bed mass [g]			Height [mm]	U_g [m/s]
	3.0 mm	2.5 mm	1.8 mm		
Characteristics of mixtures and operating conditions					
1	–	20.2	13.5	28.5	2.8 ± 0.02
2	10.6	10.6	10.6	28.5	2.8 ± 0.02

To fulfill the requirement of high spatial resolution for particle tracking, the field of view was adjusted to 100×170 mm², which corresponds to an approximate spatial resolution scale factor S_f of 7.5 pixels/mm. This factor was obtained from the standard geometry calibration process in the DaVis software. Note that only 170 mm bed height can be captured by the imaging system, as marked in Fig. 1. However, most of fluidization characteristics can be captured in this field of view.

The raw color images acquired from the high-speed camera were in the red-green-blue (RGB) space, which is defined by the three chromatic levels of red, green and blue additive primaries. In this study, the maximum number of images stored in each measurement was 5000 (5 s measurement time), which included the initial (start-up) period.

3. Color-PTV methodology

For mono-disperse granular flow in pseudo-2D fluidized beds, the methodology and applications of particle tracking velocimetry have been discussed by Hagemeier et al. (2015b) and Jiang et al. (2017b). An important aspect of PTV measurement in complex

granular flow is that both, the particle segmentation process and the particle tracking process, have strong influence on the quality and quantity of recovered particle scale information. In order to extend this technique to poly-disperse systems, colored particles were used in the measurements to identify different particle sizes, as described in Section 2.1. Therefore, a color classification was required to label particles of different sizes. In addition, a new integrated particle tracking method was introduced to ensure high performance under various fluidization conditions.

3.1. Color classification

Based on the study of Olaofe et al. (2013), classification of colored particles in the hue-saturation-value (HSV) space is easier and more accurate compared with classification in the RGB space, because the HSV representation rearranges the geometry of RGB (Cartesian) space to cylindrical-coordinate space in an attempt to be more intuitive and perceptually. Thus, raw images in the RGB space were firstly transformed into the HSV space based on standard function in MATLAB. After space transformation, the intensity in each channel of the HSV space ranged from 0 to unity.
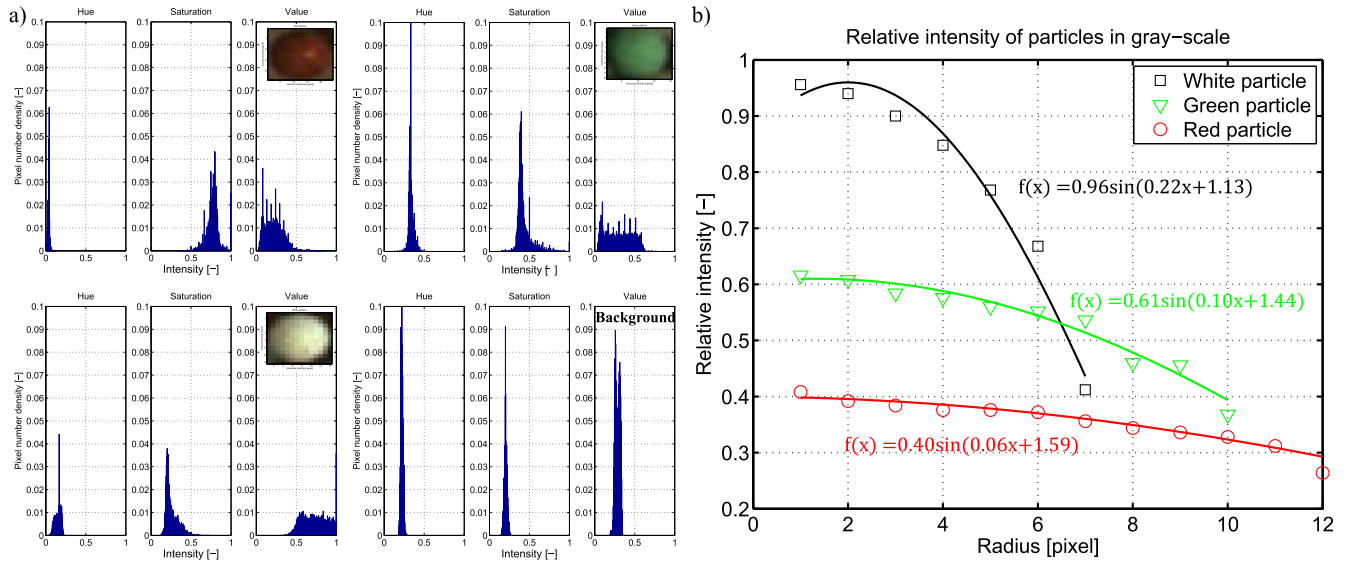
Fig. 2. The image properties of colored particles: (a) histograms of HSV channels for particles of different colors and the background; (b) mean intensity distributions in gray-scale space along radii of different color particles (Curve fits are based on the sine equation: $f(x) = a \cdot sin(bx + c)$). (For interpretation of the references to color in this figure legend, the reader is referred to the web version of this article.)

To find the characteristic of each color, statistical analysis of the three HSV channels was conducted in sampling regions with only particles of a single color (red, green or white). In this study, the size of sampling region was 100×100 pixels, and 10 different sampling regions were manually selected for each color from raw images. A similar approach was applied for the color of the background. Fig. 2(a) shows histograms of the three channels of the HSV space for different colors. In each histogram, the vertical axis relates to pixel number density and the horizontal axis is pixel intensity. It can be seen that the intensity peaks of different colors are separated. The criteria of color classification (range of thresholds) used in this work are listed in Table 2. The color red can be obviously distinguished by the saturation channel (S); whereas the colors green and white can be distinguished by the hue channel (H). Further, the information in the value channel (V) was mainly applied to distinguish the background color. After the color classification, a label matrix was generated to store flags representing four colors for each pixel of a raw image. The label matrix is impor-

Table 2
Main parameters used in Color-PTV method.

Parameter	Value	Unit
Color classification method		
Thresholds of pixel intensity in three channels (H: hue, S: saturation, V: value)		
Red	$H \in (0, 0.1), S \in (0.5, 1), V \in (0, 0.5)$	–
Green	$H \in (0.25, 0.5), S \in (0.2, 0.5), V \in (0, 0.6)$	–
White	$H \in (0, 0.2), S \in (0.2, 0.5), V \in (0.5, 1)$	–
Background	$H \in (0.1, 0.25), S \in (0.1, 0.25), V \in (0.1, 0.3)$	–
Particle segmentation method		
Template particle size	$\sqrt{2} \cdot d_p \cdot S_f / 2$	pixel
Voronoi tracking method		
Maximum displacement radius	$U_g / 2 \cdot S_f \cdot \Delta t$	pixel
Relaxation probability method		
Maximum displacement radius	$U_g / 2 \cdot S_f \cdot \Delta t$	pixel
Neighboring radius	$0.5 \cdot U_g \cdot S_f \cdot \Delta t$	pixel
Quasi-rigidity radius	$0.1 \cdot U_g \cdot S_f \cdot \Delta t$	pixel
Threshold matching probability	0.99	–

Δt is 1 ms according to the frame rate of the imaging system.

tant to accurately and quickly extract intensity information for different colors in the particle segmentation and tracking process.

Fig. 3 shows an example for the classification of three relatively similar colors (green, white and background) from *Case 1*, in which pixels belonging to white particles and green particles were respectively extracted from the raw image using the label matrix. Obviously, different colors are successfully distinguished and shapes of particles are completely retained based on the criteria spans, which is favorable to the segmentation process using particle-mask correlation method (Jiang et al., 2017b).

3.2. Particle segmentation algorithm

The particle segmentation process is performed to identify individual particle centers in PTV. After the particle segmentation, the center and the color were stored for each particle. For the particle-mask correlation segmentation, the normalized cross-correlation coefficient γ of the template particle ($m \times m$ pixels) with any interrogation region of the same size in the raw image, centered at (x, y), can be calculated by

$$\gamma(x,y) = \frac{\sum_{i=x-m/2}^{x+m/2} \sum_{j=y-m/2}^{y+m/2} [I(i,j) - \bar{I}][s(i,j) - \bar{s}]}{\sqrt{\sum_{i=x-m/2}^{x+m/2} \sum_{j=y-m/2}^{y+m/2} [I(i,j) - \bar{I}]^2 \sum_{i=x-m/2}^{x+m/2} \sum_{j=y-m/2}^{y+m/2} [s(i,j) - \bar{s}]^2}},$$
(1)

where $I(i,j)$ is the intensity in the matrix of the interrogation region in the raw image and $s(i,j)$ is the intensity in the matrix of the template particle. $\bar{I}$ and $\bar{s}$ are the space-averaged intensities of the interrogation region of the raw image and the template particle, respectively. The template particle matrix is a square matrix with the column and row size m equal to $\sqrt{2} d_p \cdot S_f / 2$ pixels (rounding to nearest integer).

The operation of Eq. (1) is based on a single matrix for every raw image, while color images include three matrices for different channels. To acquire a single matrix representing the characteristics of the color image, raw images in the RGB space were converted to gray-scale images by a luminosity method based on a weighted sum of three matrices. The weight factors were 0.299, 0.587 and 0.114 for the channels of red, green and blue, respectively (Ware, 2012). For the template particles of different sizes,
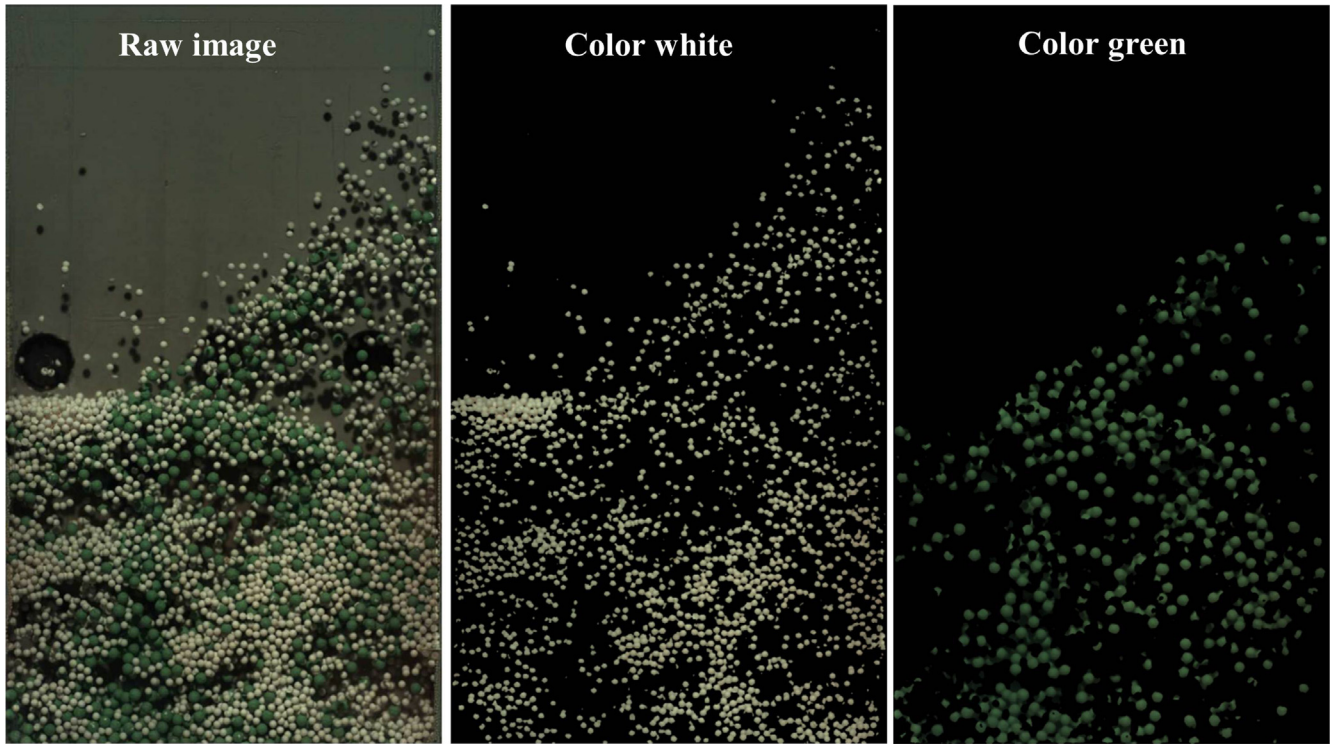
Fig. 3. Typical example of color classification (*Case 1*), including colors of white, green and background. (For interpretation of the references to color in this figure legend, the reader is referred to the web version of this article.)

the intensity features of pixels were also analyzed in gray-scale, as shown in Fig. 2(b). For each particle color, the result of relative intensity distribution along the particle radius was averaged from 10 template particles, which were manually selected from different raw images. It can be found that there are enough differences in the values and distributions of relative intensities for the segmentation of particles with different colors. The corresponding sine functions fitted from average data will be further used to generate synthetic images in the verification of the segmentation algorithm (Section 4).

3.3. Particle tracking algorithm

As discussed in the previous work (Jiang et al., 2017b), the Voronoi tracking method and the relaxation probability method both showed good performance in reconstructing particle motion in mono-disperse systems. The Voronoi method paired identical particles in two subsequent frames based on the minimum discrepancy of Voronoi first order star, which represented the favorable features of Voronoi diagram. The relaxation probability method paired identical particles in two subsequent frames based on the maximum iterated matching probability, which was related to the number of particles satisfying quasi-rigidity conditions. Since each method has its own strengths for different particle number density and fludization conditions, the tracking algorithm was switched based on a threshold solid volume fraction that was obtained by manual evaluation of sample images (Jiang et al., 2017b).

In the present study, a new tracking approach, integrating the Voronoi method and the relaxation probability method, was applied to measure particle motion in poly-disperse systems. Specifically, two tracking algorithms are separately used for each image to get two sets of tracked particle velocities; then the two data sets are merged to get final tracked velocities of individual particles. The aim of this integration is to provide a more flexible

methodology that possesses high performance under different flow conditions. Particles of different sizes are not discriminated in particle tracking to retain neighboring features that are beneficial to both individual tracking algorithms. After successfully tracking, the information about different sizes is assigned to each particle based on the results of particle segmentation. The parameters used in both, the Voronoi method and the relaxation probability method are listed in Table 2. The Voronoi tracking method only relies on the Voronoi diagram partitioning the two-dimensional Euclidean plane. The maximum displacement radius was used to speed up the algorithm. For the relaxation probability method, the relatively large neighboring radius and the relatively flexible rigidity radius were selected to accommodate the strong velocity fluctuations caused by particle–particle collisions. The relatively high threshold matching probability ensured the accuracy of evaluation. In addition, a double match filter was used in each single tracking algorithm to guarantee that the target particle in the first frame had a unique match in the second frame based on minimum displacement. More detailed descriptions of these two tracking methods can be found in Capart et al. (2002) and Baek and Lee (1996).

Based on the pairing information, the components of individual instantaneous particle velocity $\boldsymbol{v}_p$ can be calculated by particle locations at the consecutive times 1 and 2, expressed as

$$v_{p.x}(i,t) = \frac{x_2 - x_1}{\Delta t}, \quad v_{p.y}(i,t) = \frac{y_2 - y_1}{\Delta t}, \tag{2}$$

where Δt is the time step. Based on the individual particle velocity from PTV measurements, the granular temperature for a two-dimensional space Θ_{2D} can be calculated as

$$\Theta_{2D} = (\Theta_x + \Theta_y)/2; \tag{3}$$

$$\Theta_j = \frac{1}{N_p} \sum_{i=1}^{N_p} (v_{p.j}(i,t) - \langle v_{p.j}(t) \rangle)^2, \quad j = x, y; \tag{4}$$

$$\langle v_{p,j}(t) \rangle = \frac{1}{N_p} \sum_{i=1}^{N_p} v_{p,j}(i,t). \tag{5}$$

Here, N_p is the number of particles in the interrogation region used for calculating the spatial average; $v_{p,j}(i,t)$ is component j of the instantaneous velocity of individual particle i and $\langle v_{p,j}(t) \rangle$ is the instantaneous spatial average velocity in direction j. The value and distribution of granular temperature are strongly affected by the choice of interrogation region size, which actually determines the level of the influence of macroscopic bubble motion on the local microscopic particle velocity distribution; too small interrogation region size may introduce large statistical errors in the evaluation of measurements (Jiang et al., 2017b).

4. Verification of methodology by synthetic images from CFD-DEM simulation

4.1. Principle

The accuracy of measurement is a quantitative performance characteristic, expressing the agreement between a measurement result and the value of the quantity to be measured. With regards to the color-PTV measurements in fluidized beds, the measured quantity is the velocity distribution of a large number of individual particles under different fluidization conditions. According to Eq. (2), the uncertainty sources associated with the color-PTV methodology include individual particle locations (related to the particle segmentation algorithm) and the performance of particle pairing in two consecutive frames (related to both the particle segmentation algorithm and the integrated particle tracking algorithm). Whether particles can be identified and further tracked affects the global performance of color-PTV. After successful tracking, the evaluation of single particle velocity is directly influenced by the biases of particle location segmentation.

Hence, suitable criteria are essential for quantitatively evaluating the performance of the algorithms used in the proposed color-PTV methodology. First, the bias of individual location of segmented particle was used to identify the uncertainty of evaluation of individual particle velocity; this is defined as

$$L_{b,i} = \sqrt{(x_i - x_{i,t})^2 + (y_i - y_{i,t})^2}, \tag{6}$$

where (x_i, y_i) is the location vector of segmented particle i, and $(x_{i,t}, y_{i,t})$ is its true location vector. Following the works of Baek and Lee (1996) and Hassan et al. (1992), the segmentation ratio, the recovery ratio and the error ratio were used as criteria to verify the global performance of the particle segmentation algorithm and the integrated particle tracking algorithm. Specifically, the segmentation ratio R_s is defined as

$$R_s = \frac{number\ of\ segmented\ particles}{maximum\ number\ of\ possible\ particles}; \tag{7}$$

the recovery ratio R_r is defined as

$$R_r = \frac{number\ of\ accurately\ recovered\ vectors}{maximum\ number\ of\ possible\ vectors}; \tag{8}$$

and the error ratio R_e is defined as

$$R_e = \frac{number\ of\ error\ vectors}{total\ number\ of\ recovered\ vectors}. \tag{9}$$

However, it is difficult to directly acquire all quantities necessary in order to apply criteria from a large number of particles with complex motion by experiments. Therefore, data from CFD-DEM simulations, performed according to the experimental configuration and operating conditions, were instead used to verify the color-PTV methodology in the present work. The basic idea was similar to the synthetic (standard) images approach for evaluating PIV algo-
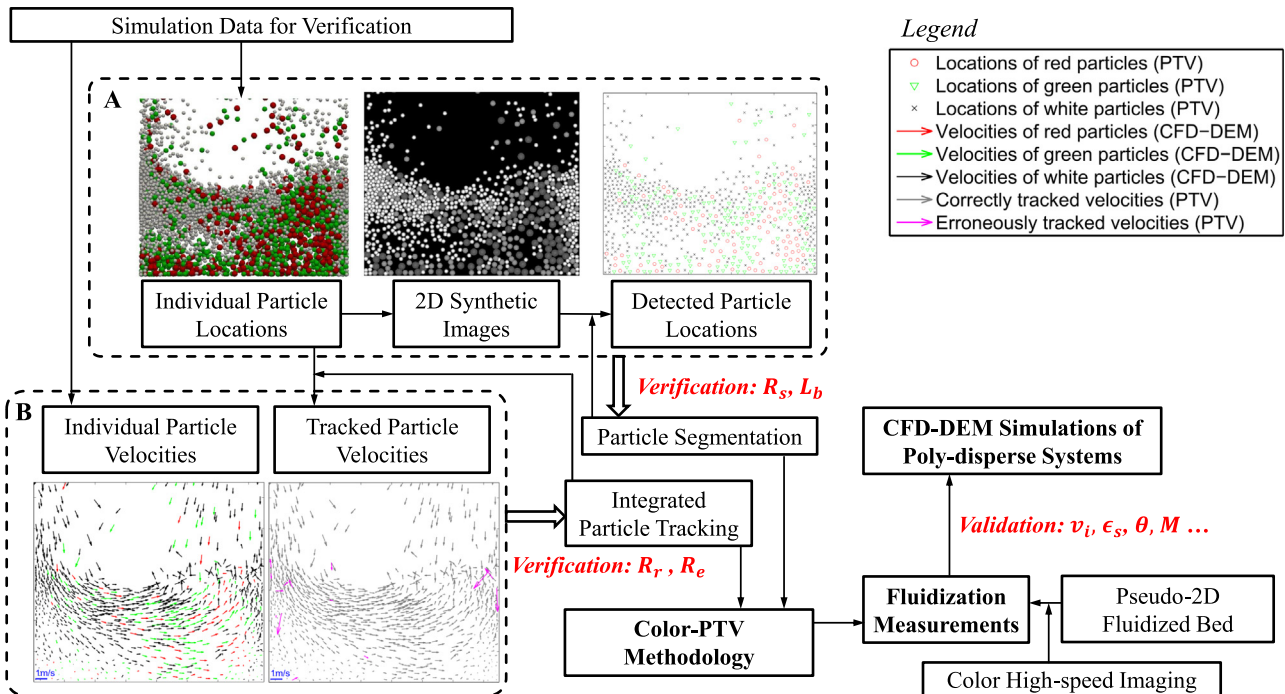

Fig. 4. Schematic representation of the two-way verification/validation of PTV measurement and CFD-DEM simulation: (block A) illustrates the verification of the particle segmentation algorithm based on R_s and L_b; (block B) describes the verification of the integrated particle tracking algorithm based on R_r and R_e (erroneously tracked vectors are marked in magenta to distinguish from correct vectors in the right sub-figure). The verified color-PTV methodology can be applied to images from fluidization measurements to validate corresponding CFD-DEM simulations. (For interpretation of the references to color in this figure legend, the reader is referred to the web version of this article.)

rithms (Okamoto et al., 2000; Lecordier et al., 2001; de Jong et al., 2012). The main advantages in using CFD-DEM simulation data are:

1. As a well established simulation method, CFD-DEM can properly describe the motion of particles in granular systems.
2. CFD-DEM simulation data can represent particle motion under different fluidization conditions.
3. All required variables in Eqs. (6)–(9) can be easily retrieved from CFD-DEM data.

Therefore, the use of CFD-DEM simulation data is complementary to real experimental images because it is a powerful approach to investigate the effects of associated parameters (such as solid volume fraction, particle velocity and granular temperature) on the accuracy of particle velocity measurement, as well as to estimate the intrinsic limitations of the methodology.

Fig. 4 shows the flow diagram of verification of the color-PTV methodology based on synthetic images generating from simulation data, including block A for particle segmentation and block B for integrated particle tracking. After verification, the color-PTV methodology can be used to evaluate particle dynamics and mixing behavior based on color images acquired from fluidization measurements in the pseudo-2D fluidized bed. In addition, measurement data can be used to validate corresponding CFD-DEM simulations of poly-disperse particle systems.

Corresponding to block A, synthetic images were generated to evaluate the performance of the segmentation algorithm by means of the bias L_b and the segmentation ratio R_s. In order to be close to pseudo-2D conditions, only particles in the first layer were selected from three-dimensional CFD-DEM simulation data to generate two-dimensional synthetic images, which means that the normal distances from the centers of selected particles to the front wall were smaller than 3 mm. According to the descending order of the distances to the front wall, contours of individual particles with different sizes were created in each image based on the corresponding relative intensity distribution from Fig. 2(b). By this approach, the overlap between particles that is encountered in measurement images was intentionally introduced to inspect its effect on the particle segmentation. According to the analysis of measurement images, 0.1% noisy pixels were randomly introduced to fit the real image quality. In terms of spatial resolution, the grayscale synthetic image was the same as the raw image from measurements. Based on the particle-mask correlation segmentation, three template particles were separately used to process each synthetic image and to obtain the segmented locations of particles with different sizes. Then, the bias L_b and the segmentation ratio R_s were evaluated by the comparison of individual particles.

Corresponding to block B, the integrated particle tracking algorithm was verified by means of the recovery ratio R_r and the error ratio R_e. Using a unique identification number (ID) of each particle in the DEM solver, particle velocities can be easily evaluated from the location of each individual particle before and after a time step (Eq. (2)). However, a sequential labeling process was required to extract the pairing information that obtained form integrated PTV method. In the first frame, unique IDs were assigned to all segmented particles. After successful pairing, each matched candidate particle in the second frame received the same ID as in the first frame. The candidate particle without a valid pair received a new ID. Then, tracked particle velocities can be also evaluated by Eq. (2). The process was repeated for all image sequences to obtain the trajectories of all individual particles. In order to gain the numerators in Eqs. (8) and (9), particle velocities in the same time step obtained from PTV and CFD-DEM were compared one by one according to the locations and the lengths of vectors.

The thorough analysis of segmentation ratio, recovery ratio and error ratio with respect to particle velocity, solid volume fraction

and granular temperature can be further conducted to assess the applicability of the color-PTV method to measure the dynamics of poly-disperse particle systems in different fluidization conditions.

4.2. CFD-DEM simulation

OpenFOAM and LIGGGHTS (Goniva et al., 2012) were used to conduct the CFD-DEM simulations based on same operation conditions and particle properties as in the measurements. Governing equations are summarized in Table A.1. All models and boundary conditions used were previously published, e.g. Zhu et al. (2007), Zhou et al. (2010), Goniva et al. (2012) and Jiang et al. (2017a). Some numerical techniques were described by Link et al. (2005), Zhu et al. (2007) and Goniva et al. (2012).

In CFD-DEM coupling, the momentum exchange between the solid phase and the fluid phase, characterized by the momentum exchange coefficient β_{pf}, can be calculated by various drag models. A detailed overview of drag force equations for mono-disperse and poly-disperse systems was given by Beetstra et al. (2007b). The drag force $\boldsymbol{f}_{d,i}$, due to the fluid-solid friction at the surface of particles, can be evaluated on the single particle scale. An accurate drag model is of great importance for the performance in the prediction of complex particle-fluid flows, especially in poly-disperse systems. In the example of a binary system, if the volume fraction of small particles is somewhat smaller than the averaged solid volume fraction (including both large and small particles), then an over-prediction of the drag force on small particles results. Inversely, the drag force is under-predicted for the large particles. A correction for the effect of poly-dispersity, as listed in Table 3, was essential to improve the accuracy of simulations, as discussed by Beetstra et al. (2007b,a). The correction factor depends on the solid and fluid volume fractions (ϵ_s and ϵ_f), and on the ratio y_i of the diameter of a certain class of particles $d_{p,i}$ and the Sauter mean diameter of the entire particle system d_{32}. The drag model expressed by Eq. (18) was used in the CFD-DEM simulation to obtain data for verification of the color-PTV methodology.

The physical properties and simulation parameters are listed in Table 4. Particle interactions were calculated by the Hertzian contact model with tangential history tracking (Di Renzo and Di Maio, 2004). The equations of the contact model are summarized in Table A.2. In this soft-sphere contact model, the effect of spring and dash-pot appear through stiffness k and damping coefficient η, which were determined by the physical material properties of Poisson ratio σ, Young's modulus E and the coefficient of restitution e. The coefficients of restitution for particle-particle interaction and particle-wall interaction were considered identical in this study. The particles were assumed to be less stiff than they are in reality, in order to avoid the requirement to use excessively small DEM time steps. The Young's modulus of 10^8 Pa was used in this study, which provided negligible differences as compared to the simulation with the typical Young's modulus of 10^{10} Pa of γ-alumina particles (Müller et al., 2013). Artificial softening of particles is universally used in CFD-DEM simulations of gas-solid flow in fluidized beds, because the effect of stiffness on particle motion is secondary compared with the particle-fluid interactions (Tsuji et al., 1993; Kuo et al., 2002; Yang et al., 2014; Boyce et al., 2017). Coulomb's friction law was applied to account for particle sliding, in which the friction coefficient μ_f was taken from Fries et al. (2013). The rolling coefficient k_r in the directional constant rolling friction model (Ai et al., 2011) was taken from Goniva et al. (2012).

The chamber was divided into $20 \times 100 \times 3$ cells in x, y and z directions, respectively. The size ratio d_{cell}/d_{32} was approximately 2.3 for both simulated cases, where $d_{cell} = \sqrt[3]{V_{cell}}$ was an effective

Table 3
Particle-fluid interactions models.

Momentum exchange coefficient β_{pf} (14)
$$\beta_{pf} = \frac{18\mu_g \epsilon_s \epsilon_f}{d_p^2} F(\epsilon_s, Re_p)$$
Drag force on individual particle $\boldsymbol{f}_{d,i}$ (15)
$$\boldsymbol{f}_{d,i} = \frac{V_{p,i}}{\epsilon_s} \beta_{pf} (\boldsymbol{u} - \boldsymbol{v}_{p,i})$$
Mono-disperse system (Beetstra et al., 2007b)
Normalized drag force $F_{mono}(\epsilon_s, Re_p)$ (16)
$$F_{mono} = \frac{10\epsilon_s}{\epsilon_f^2} + \epsilon_f^2(1 + 1.5\epsilon_s^{0.5}) + \frac{0.413 Re_p}{24\epsilon_f^2}\left[\frac{\epsilon_f^{-1} + 3\epsilon_s\epsilon_f + 8.4 Re_p^{-0.343}}{1 + 10^{3\epsilon_s} \cdot Re_p^{-(1+4\epsilon_s)/2}}\right]$$
Reynolds number of particle Re_p (17)
$$Re_p = \frac{\epsilon_f \rho_f |u - v_{p,i}| d_p}{\mu_f}$$
Poly-disperse system (Beetstra et al., 2007a)
Normalized drag force $F(\epsilon_s, Re_p)$ (18)
$$F = F_p \cdot F_{mono}$$
with d_{32} instead of d_p in Eq. (17) and correction factor for the effect of size dispersity F_p (19)
$$F_p = \epsilon_f y_i + \epsilon_s y_i^2 + 0.064\epsilon_f y_i^3$$
Sauter mean diameter d_{32} (20)
$$d_{32} = \frac{\sum_{i=1}^c N_i d_{p,i}^3}{\sum_{i=1}^c N_i d_{p,i}^2}$$
Diameter ratio y_i (21)
$$y_i = \frac{d_{p,i}}{d_{32}}$$

Table 4
Physical properties and simulation parameters.

Parameter	Value	Unit
Simulation chamber		
Dimensions in x, y, z directions	$100 \times 340 \times 14$	mm
Grid numbers in x, y, z directions	$20 \times 100 \times 3$	–
Size ratio d_{cell}/d_{32}	2.3	–
	2.0, 2.7 (independence study)	–
Particle phase		
Contact model: hertzian, inelastic, with friction, rolling and tangential history		
Particle diameter d_p	Table 1	mm
Particle density ρ_p	Table 1	kg/m³
Coefficient of restitution e	Table 1	–
Young's modulus E	10^8	Pa
Poisson ratio σ	0.25	–
Friction coefficient μ_f	0.1	–
Rolling coefficient k_r	0.1	–
Gas phase		
Gas density	1.2	kg/m³
Dynamic viscosity	1.84×10^{-5}	Pa·s
Superficial gas velocity	2.8	m/s
Boundary condition	*Slip*	–
Coupling simulation parameters		
CFD time step Δt_{CFD}	5×10^{-5}	s
DEM time step Δt_{DEM}	10^{-6}	s
Simulation time t_{sim}	30	s

length based on the volume of each CFD cell. For the purpose of examination of grid independence (results shown in Section 5), two further CFD grids with size ratios of 2.0 (finer grid) and 2.7 (coarser grid) were also built.

The accurate simulation of granular flow in fluidized beds is very sensitive to the correct calculation of cell solid volume fraction (Peng et al., 2014). According to the size ratio of 2.3, the solid volume fraction was calculated by the "divided" method (Goniva et al., 2012), which generated smooth solid volume fraction fields. In this method, particles are first divided to equal small parts by a series of distributed marker points. Then, the portion of particle volume located in a certain CFD cell is calculated from the number of respective marker points.

The time step should be set smaller than a critical value to conform with physical laws and guarantee stability of the DEM and CFD solvers. In the CFD, the Pressure-Implicit with Split-Operator (PISO) pressure-velocity coupling algorithm was used to solve the Navier-Stokes equations for unsteady flow. The k-ϵ model

was applied to simulate mean flow characteristics for turbulent conditions. The CFD time step was set to 5×10^{-5} s, which ensured that the maximum Courant number was less than 0.5. The collision time τ_H can be estimated based on Hertz contact theory (Kobayashi et al., 2013), expressed as:

$$\tau_H = 2.87\left(\frac{m_{eq}^2}{R_{eq}E_{eq}^2 v_{c,max}}\right)^{0.2}. \tag{10}$$

Assuming a maximum collision velocity $v_{c,max}$ of 1.5 m/s in the whole bed (Jiang et al., 2017b), the estimated collision time τ_H for two 1.8 mm particles (the smallest objects occurring in the system) is approximately 2.6×10^{-5} s. Hence, the DEM time step was selected as 10^{-6} s, less than $\tau_H/20$ for the entire granular system, to ensure an accurate performance of the contact model. The coupling interval between DEM and CFD solvers was 50 times the DEM time step.

CFD-DEM simulation data of *Case 2* with Eq. (18) (ternary mixture), extracted from 0 to 30 s with an interval of 1 ms, were used to verify the color-PTV methodology. The extraction interval was the same as the interval between two subsequent image frames in real measurements. Similarly to the start-up period in the real measurement, the superficial gas velocity in the simulation was linearly increased from 0 to 2.8 m/s in the time period of 1 s. In order to include a wider range of particle dynamics, data was extracted from the simulation for verification at more points (in time) than in the real measurement.

4.3. Verification of segmentation algorithm

Fig. 5 shows the cumulative distributions of bias $L_{b,i}$ of individual segmented locations according to statistical analysis of approximately 2.5×10^7 particles. Due to the discrete nature of digital images, possible bias values were 0, 1, $\sqrt{2}$, 2, $\sqrt{5}$, $\sqrt{8}$, and 3 pixels. When the segmented particle location coincides with the corresponding particle location in DEM data, the bias $L_{b,i}$ is zero. Generally, the particle-mask correlation segmentation algorithm shows good performance for particles with different sizes. More than 89% of all particles can be identified without any error. The cumulative
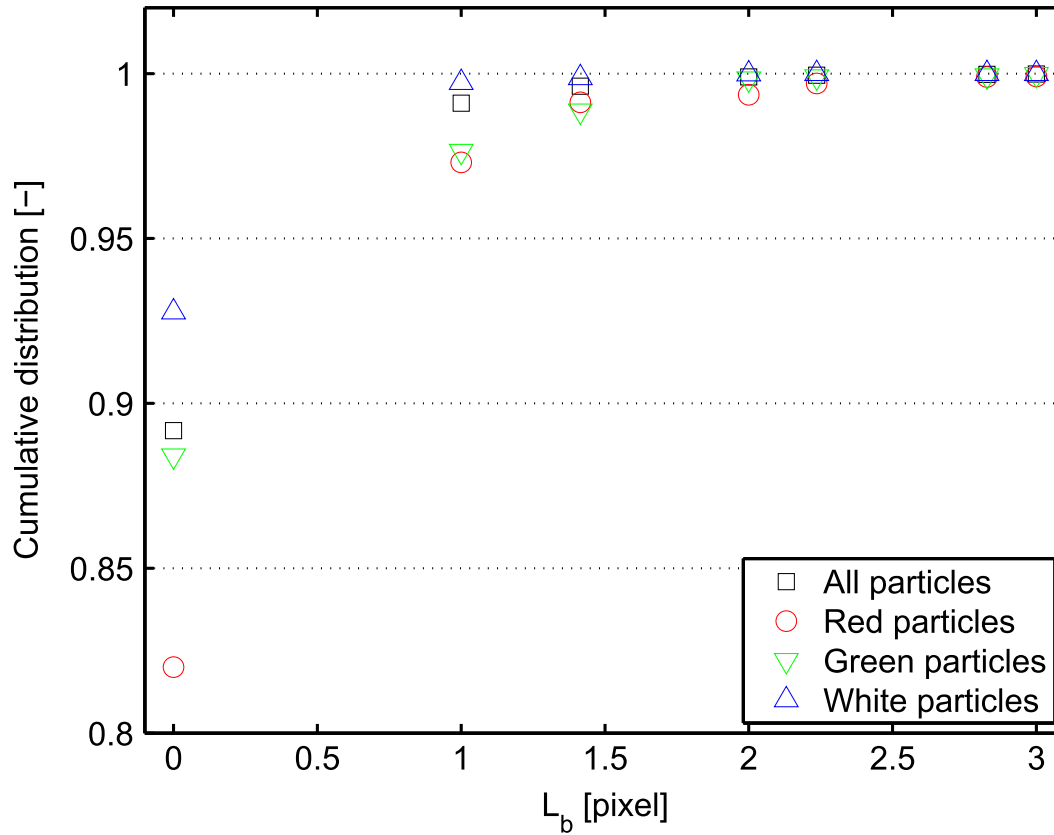
Fig. 5. Cumulative distribution of the bias of particle-mask correlation segmentation (statistical analysis of approximately 2.5×10^7 particles).

distributions for all particles reaches unity at $\sqrt{8}$ pixels, which indicates the high precision of particle segmentation. Smaller particles are more accurately located compared with larger particles. The mean values of bias $L_{b,i}$ of all particles, red particles, green particles and white particles were 0.11, 0.31, 0.13, and 0.07 pixel, respectively.

For the particle-mask correlation approach, the segmentation ratio was mainly influenced by the solid volume fraction that was calculated as the ratio of the total particle volume to the volume of the investigation region. To this end, the full image was divided into small investigation regions with a size of 75×75 pixels, and an overlap of 2/3 was set between two neighboring regions to obtain better spatial resolution. The depth of investigation region was considered as the Sauter mean diameter d_{32} in this study. This method of partitioning the investigation region will be used in all following post-processing. For the case of verification study, the mean value of solid volume fraction was 0.136 with a standard deviation of 0.120 for all data from 30 s simulation time.

Fig. 6(a) shows the segmentation ratio R_s for all three sizes of particles with respect to solid volume fraction ϵ_s. The points are averages, where the two dash lines define the region covered by the standard deviation of data. Globally, the segmentation ratio for all particles is close to unity when the solid volume fraction is lower than 0.2. Then, there is a decreasing tendency of the segmentation ratio when the solid volume fraction further increases from 0.2 to 0.5. The standard deviation of segmentation ratio experiences a similar tend: it is small when the solid volume fraction is smaller than 0.2 and gradually increases after the solid volume exceeds 0.2. In fact, the standard deviation can be considered as a quantification of precision in respect to the random errors of measurements. Reasonably, the inevitable overlap of particles in the dense region led to a decrease of segmentation ratio and an

increase of the corresponding standard deviation, since the segmentation algorithm depends on intensity distribution on the surface of individual particles.

Fig. 6(b) shows the influence of different sizes (colors) on the segmentation ratio. Obviously, the smaller the particle size, the better the performance of particle segmentation, because the gray-scale intensity distribution on the surface of small particles is more pronounced compared to other particles (as shown in Fig. 2(b)). In other words, the more pronounced the intensity distribution, the less is the interference of overlap of particles with the segmentation algorithm.

Nevertheless, the particle segmentation algorithm shows very good accuracy and precision in the primary range of solid volume fraction. For the largest solid volume fraction, the lowest value of segmentation ratio of red particles is still larger than approximately 0.75. Notably, the intensity of individual particles is also affected by the shadowing effect of neighboring particles and the motion blur effect in real fluidization measurements, which were not included in the current verification study of particle segmentation. There should be a certain decrease in segmentation ratio to take account of these two negative effects in real measurements.

4.4. Verification of integrated tracking algorithm

Fig. 7 shows the influence of different tracking algorithms on the recovery ratio with respect to solid volume fraction. The Voronoi method is more suitable in the dense region, in terms of both accuracy and precision. However, if the solid volume fraction is lower than 0.2, there is a large decrease in recovery ratio. In the dilute region, the mean free paths of neighboring particles (the extremities of Voronoi first order stars) are relatively large. Hence, the loss of single particles in the dilute region, caused by motion in
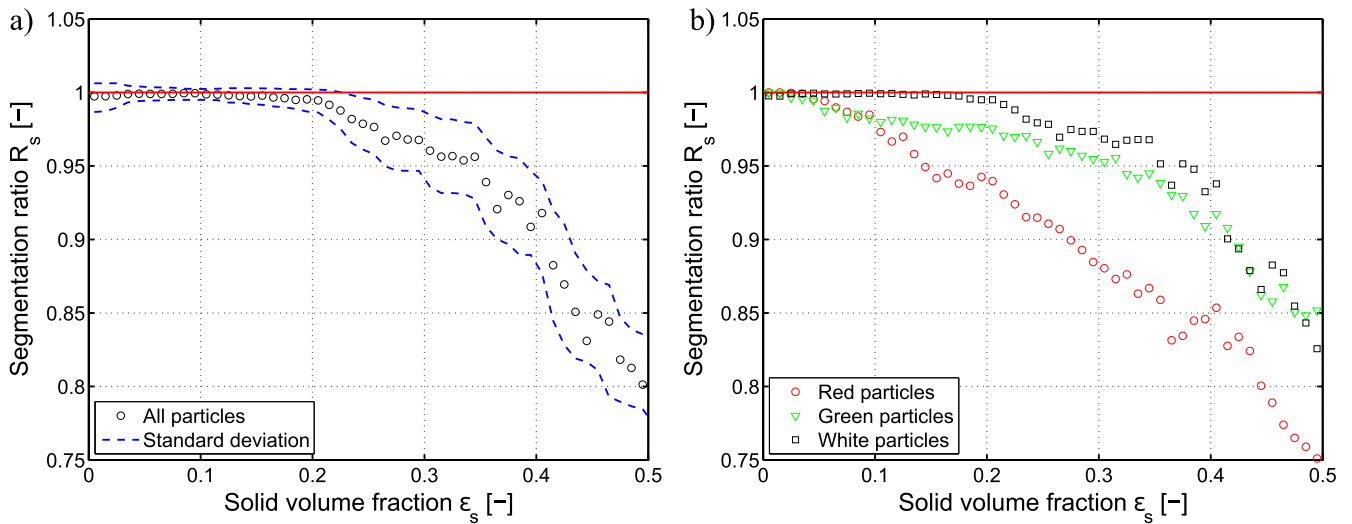
Fig. 6. Segmentation ratio R_s: (a) all particles with standard deviation, (b) particles of different sizes (colors). (For interpretation of the references to color in this figure legend, the reader is referred to the web version of this article.)
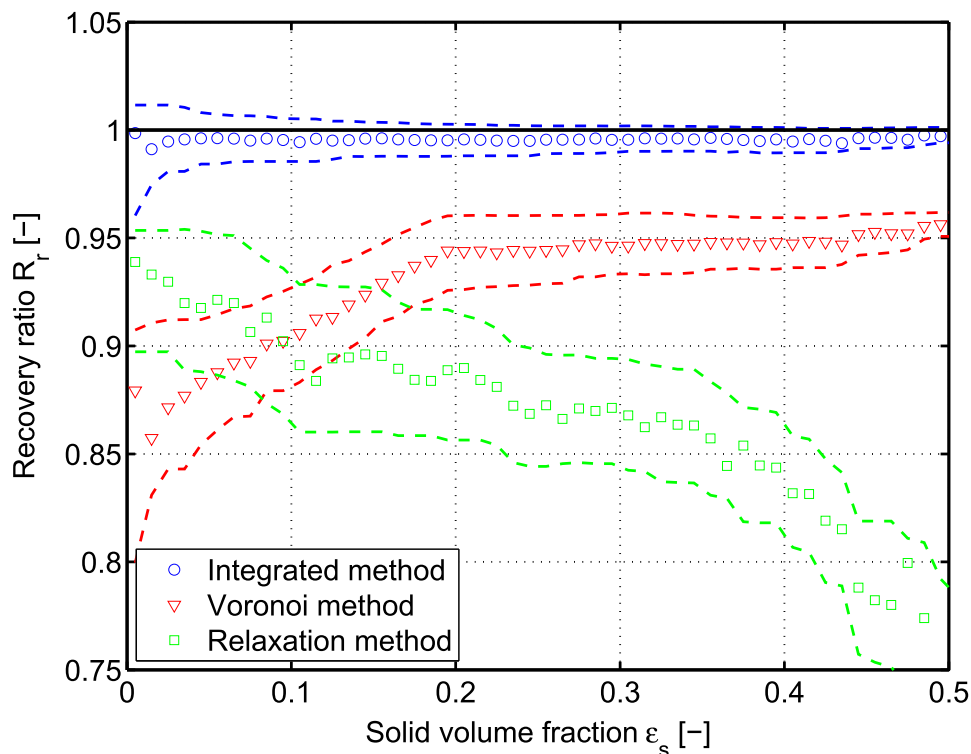

Fig. 7. Comparison of recovery ratio R_r from the integrated tracking method, the Voronoi tracking method and the relaxation probability tracking method (standard deviations for the different methods are labeled by two dashed lines of corresponding colors). (For interpretation of the references to color in this figure legend, the reader is referred to the web version of this article.)

third direction vertically to the front wall, can generate relatively large discrepancies of several nearby Voronoi first order stars, compared to the discrepancies generated by the in-plane motion of particles. This instability of Voronoi first order stars may cause erroneous pairing of target particles in the dilute region. However, the negative effect of this instability is very small in the dense region due to the naturally shorter mean free paths.

In case of the relaxation probability tracking method, the recovery ratio decreases gradually with increasing solid volume fraction, whereas the standard deviation is larger than that of the Voronoi

method for most solid volume fractions. Remarkably, the Voronoi method and the relaxation method are complementary in terms of the recovery ratio, especially in the dilute region (solid volume fraction smaller than 0.1). As a consequence, the final recovery ratio obtained by the integrated tracking method is very close to unity in almost the entire range of solid volume fractions. Moreover, the standard deviation of the integrated tracking method is smaller than that of either single tracking method. Hence, use of the integrated particle tracking helps to achieve high performance for all solid volume fractions. For all three tracking methods, the
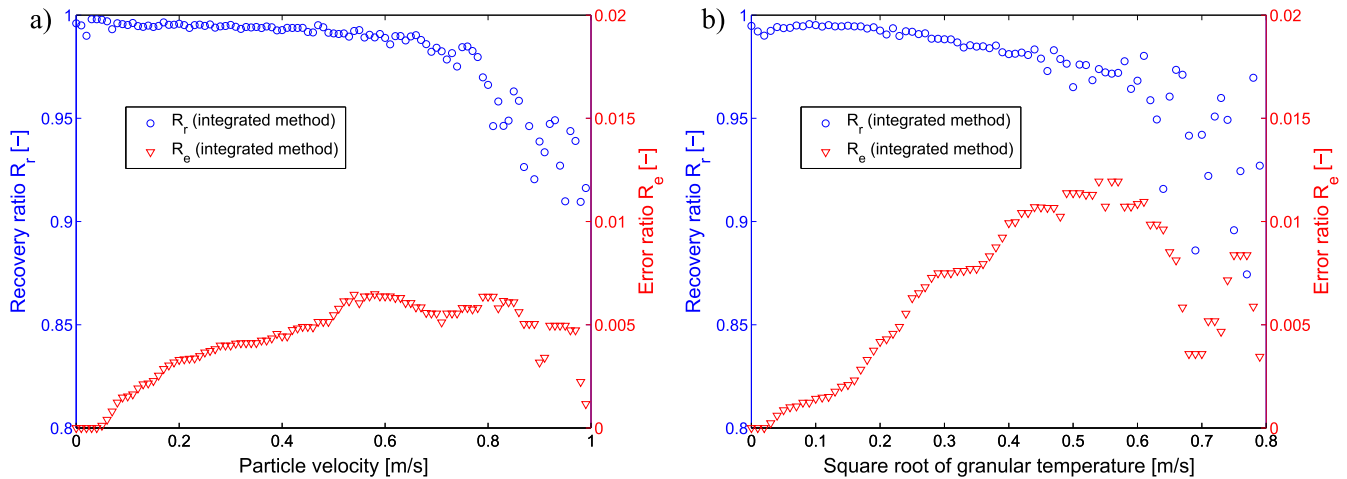
Fig. 8. Recovery ratio R_r and error ratio R_e: (a) influence of particle velocity, (b) influence of particle granular temperature.

error ratio was lower than 0.005 and had no apparent dependence on the solid volume fraction.

It should be noted that the recovery ratio and error ratio were not only influenced by the solid volume fraction, but were also significantly affected by the local particle dynamics such as particle velocity and particle granular temperature. For the parameters of the verification study, the mean value of particle velocity was 0.311 m/s with a standard deviation of 0.206 m/s; and the mean value of the square root of particle granular temperature was 0.132 m/s with a standard deviation of 0.084 m/s.

Fig. 8(a) shows the recovery ratio (left y axis) and the error ratio (right y axis) with respect to the local average particle velocity (magnitude) from the integrated method. When the particle velocity exceeds approximately 0.7 m/s, the recovery ratio evaluated by the integrated method deviates from desired value of unity and becomes more scattered. The error ratio slowly increases to a maximum value of approximately 0.006 as the particle velocity increases from 0 to 0.7 m/s. Fig. 8(b) shows the recovery ratio and the error ratio with respect to the local average square root of particle granular temperature. When the square root of particle granular temperature increases from 0 to 0.6 m/s, the recovery ratio decreases from unity to 0.95; and the error ratio increases from 0 to 0.012. As the square root of particle granular temperature further increases, large fluctuations appear in both the recovery ratio and error ratio due to the low number of samples in this range. Based on statistical analysis, only a tiny fraction (less than 1%) of the investigation regions can experience velocity larger than 0.7 m/s or square root of granular temperature larger than 0.6 m/s. In total, the integrated particle tracking algorithm was able to achieve very good recovery ratio in most of operating conditions. The increase of error ratio with increasing local particle velocity and granular temperature can be explained by the decrease of stability of neighboring structures associated with the mean free path (solid volume fraction).

According to the verification results, the color-PTV methodology can identify and track particles of different sizes with high accuracy and precision. Remarkably, the final recovery ratio obtained by the integrated tracking method is very close to unity for all solid volume fractions due to the good complementarity of Voronoi and relaxation probability tracking. Since the well-established CFD-DEM simulation can provide very similar fluidization conditions as observed in real measurements, including the solid volume fraction, the local velocity and the local particle granular temperate, measurements of poly-disperse particle dynamics using the color-PTV methodology are expected to be reasonably

trustworthy. Moreover, CFD-DEM simulation data can be very useful in designing experiments and optimizing the parameters of the segmentation and the tracking algorithms. In order to achieve high segmentation ratio and low bias, the size of template particle in the segmentation can be adjusted according to the characteristics of intensity distribution. The frame rate of the high-speed camera has to be increased when insufficient recovery ratio appears in the primary ranges of solid volume fraction, particle velocity and granular temperature. In the present work, the parameters listed in Table 2 have been optimized based on such preliminary studies.

5. Results and discussion

We will present results from color-PTV measurements of *Case 1* (binary mixture) and *Case 2* (ternary mixture), in form of the time-averaged particle volumetric flux, distributions of individual particle velocity, distributions of particle granular temperature and the mixing index. In addition, comparisons with CFD-DEM simulations using two drag models with (Eq. (18)) or without (Eq. (16)) correction for poly-dispersity will be conducted. It is noted that only particles in the first layer were extracted from simulation data to be close to pseudo-2D conditions of measurements. Specifically, the normal distances from the centers of particles to the front wall were smaller than 3 mm. On the basis of visual observations, the flow in both investigated cases can be assigned to the slugging regime, with separated slugs (bullet-shaped voids) and bubbles filling the entire cross-section of the pseudo-2D fluidized bed. Turbulent fluidization flow regime was not observed in either of the two cases.

5.1. Particle volumetric flux

As discussed by Tang et al. (2016) and Jiang et al. (2017b), the time-averaged particle velocity profiles can be spurious to describe particle circulation pattern, because the contribution of few particles with really high velocity to the global motion of particles is overestimated in the dilute region. Therefore, the volumetric flux of particles, i.e. the volume flow rate per unit area m³/(m² · s), was evaluated to accurately reveal the global particle circulation motion. With regard to PTV measurements, the volumetric flux of particles was calculated by the product of solid volume fraction and average particle velocity in each investigation region. The size and arrangement of investigation regions is the same as in the verification study.

The size of CFD grid may affect the mapping and evaluation of solid volume fraction field and the numerical solution of turbulent gas flow with solid particles. Clearly, grid independence needs to be established, before one can conduct the qualitative or quantitative analysis of CFD-DEM simulations in confidence. The study of grid independence was performed only using the drag model with correction for size dispersity in *Case 1*. Fig. 9(a) shows the time-averaged particle volumetic flux profiles over 5 s from the measurement and simulations with three sets of CFD grid. The data points are averaged from investigation regions in a height range of 450–525 pixels and are assigned to the right boundary of inves-

tigation region in x axis. The simulations with three different grid sizes predict almost the same profiles of volumetric particle flux in both the vertical and the horizontal direction. Therefore, the CFD grid with size ratio d_{cell}/d_{32} of 2.3 was used together with the "divided" void-fraction approach in this study.

Fig. 9(c) shows the results of time-averaged particle circulation for *Case 1*, and the vector for time-averaged particle volumetric flux is assigned to the bottom right corner of each investigation region. Obviously, two nearly symmetric vortices can be observed in the results of both the experiment and the simulation (Eq. (18)), which implies that 5 s time is enough to investigate the circulation
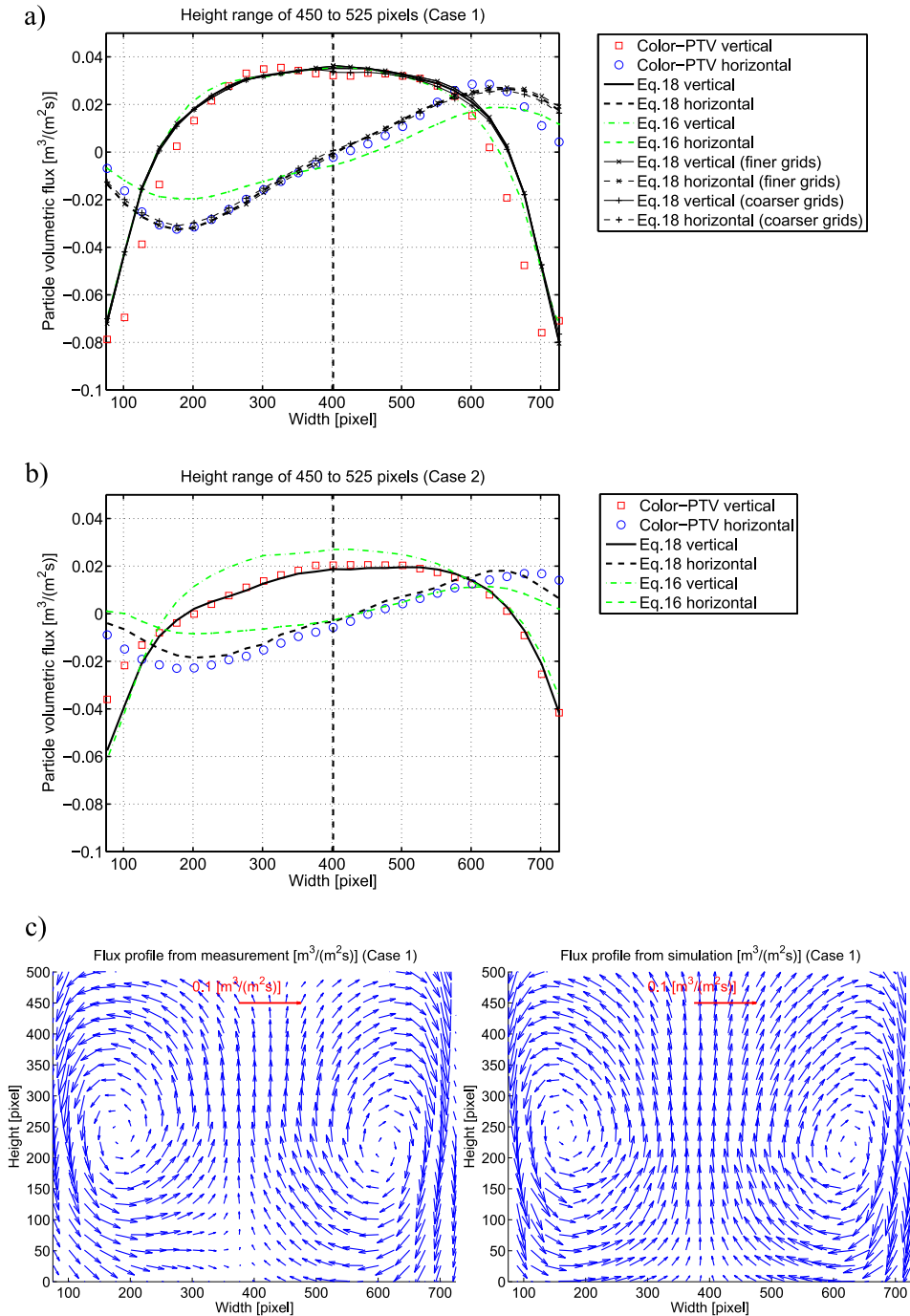

Fig. 9. Time-averaged particle volumetric flux: (a) profiles in vertical and horizontal directions for *Case 1* at a height range of 450–525 pixels, together with the results of grid independence study for three CFD grids, (b) profiles for *Case 2* at a height range of 450–525 pixels and (c) global circulation patterns for *Case 1* from the experiment and the simulation (Eq. (18)).

motion in this pseudo-2D fluidized bed. Only minor difference exists between the heights of the centers of the two vortices obtained from the experiment and the simulation. The center of the left vortex is located at a height of about 240 pixels, and the center of the right vortex is located at about 220 pixels. The top boundary of the two vortices starts to form at a height of about 450 pixels, which is also the stably fluctuating height of the dense bed surface. Bubbles or slugs erupt at this surface, accelerating particles into the free-board and resulting in horizontal transport towards the side walls. Globally, particles are transported upwards in the center of bed and slide downwards close the side walls, which is associated with the inception, coalescence and eruption of traveling bubbles or slugs at different heights of the fluidized bed. However, it is important to note that instantaneous flow patterns may differ significantly from the time-averaged circulation pattern due to the strongly chaotic motion of bubbles and particles. This result for particle circulation is very similar to published observations for mono-disperse systems using PIV and PTV measurements (Laverman et al., 2008; Tang et al., 2016; Jiang et al., 2017b). The global particle circulation for *Case 2* also shows two nearly symmetric vortices, but their centers were located lower compared to *Case 1* (not shown in the figure).

The results from Eqs. (16) and (18) in Fig. 9(a) shows that the accuracy of simulation is improved by correction for size poly-dispersity, especially in the horizontal direction. Obviously, the simulation using Eq. (16) underestimates the horizontal transport of particles due to eruptions of bubbles or slugs near the dense bed surface. In this context, it should be noted that the height range of 450–525 pixels was somewhat higher than the upper surface of the fluidized bed. The variation trend in the horizontal direction of all methods indicate the approximate reflection symmetry of the two vortices. However, the simulation with Eq. (18) underestimates the motion of particles sliding downwards the side walls. As shown in Fig. 9(b), the general shapes of profiles are similar with *Case 1*. The decreases of particle volumetric fluxes in both horizontal and vertical directions were caused by the reduces of heights of two vortices.

5.2. Distributions of particle velocity and particle granular temperature

The superiority of color-PTV measurement lies in its ability to reconstruct instantaneous velocities of particles with different sizes. Hence, the comparisons of density distributions of the individual velocities of particle with different sizes were performed in both vertical and horizontal directions, as shown in Fig. 10. The density distributions were evaluated by particles appearing at heights ranging from 450 to 525 pixels at all time steps. The total number of time steps is 5000 for both experiments and simulations. From the measurement results, the transport of all particles in the vertical direction is stronger than that in the horizontal direction at this bed height. The density distributions are approximately symmetric with respect to the vertical center line. In this height range, the velocities of small particles are slightly larger than those of large particles in the vertical direction; and, inversely, the velocities of small particles are slightly lower in horizontal direction. The differences of particle velocities in both vertical and horizontal directions are relatively small at this height range, compared with the profiles of volumetric flux in Fig. 9(a) and (b). Most of results from simulations using Eq. (18) are more conform to the measurement results, compared with the drag model without correction for the effect of size poly-dispersity. This correction improved the agreement with measurement results by avoiding the over-estimation of drag force for small particles and the under-estimation of drag force for large particles.

On the basis of Eqs. (3)–(5), the color-PTV measurement can also provide distinguishable information about particle granular temperature for particles with different sizes. The particle granular
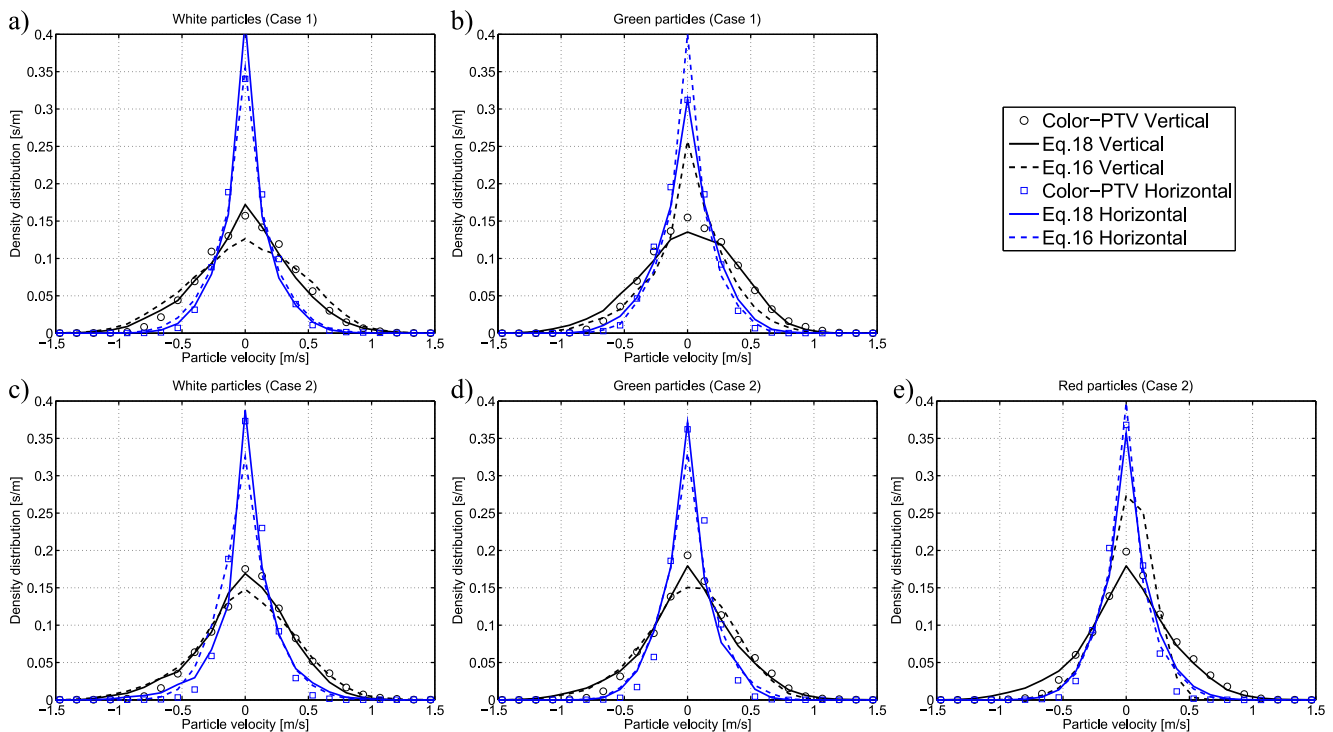

Fig. 10. Comparisons of density distributions of the individual particle velocity (including vertical and horizontal directions) at a height range of 450–525 pixels: (a) white particles of *Case 1*, (b) green particles of *Case 1*; (c) white particles of *Case 2*, (d) green particles of *Case 2* and (e) red particles of *Case 2*. (For interpretation of the references to color in this figure legend, the reader is referred to the web version of this article.)
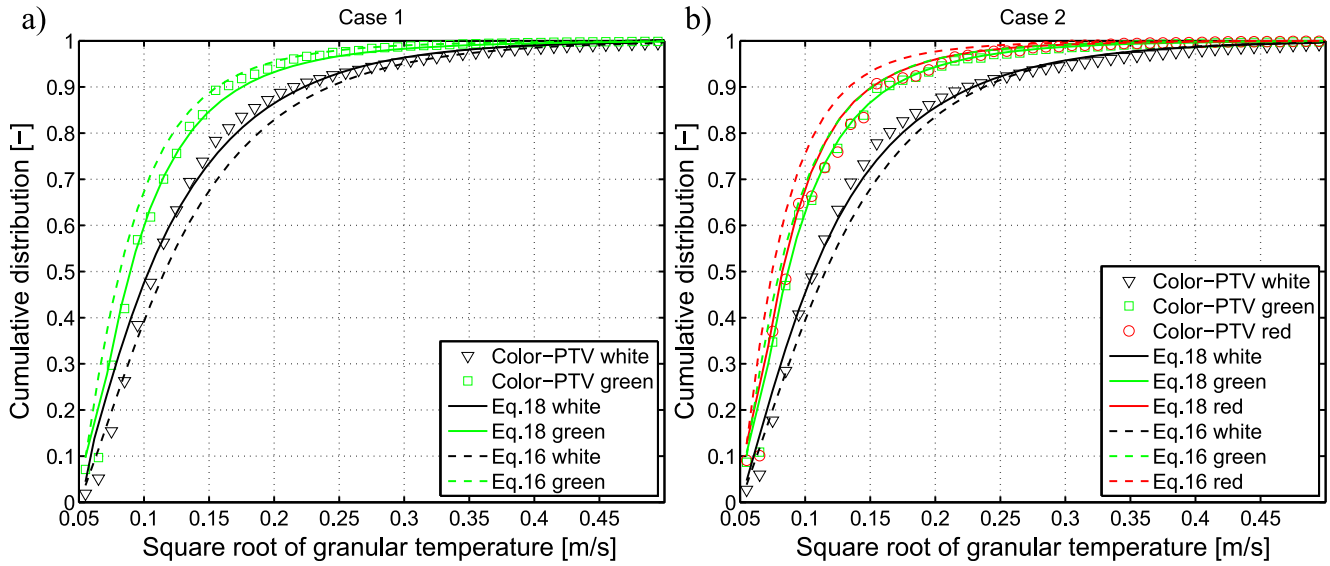
Fig. 11. Comparisons of cumulative distributions of the square root of granular temperature for different classes of particles in the entire field of view: (a) white and green particles for *Case 1* and (b) white, green and red particles for *Case 2*. (For interpretation of the references to color in this figure legend, the reader is referred to the web version of this article.)

temperature corresponds to the relative velocity of particles that may drive diffusive mixing and particle collisions. Fig. 11(a) shows the comparison of cumulative distributions of the square root of particle granular temperature of different particles for *Case 1*. Different to Fig. 10, the cumulative distributions were obtained from all investigation regions in the field of view at all time steps. According to the color-PTV measurement, the granular temperature of small particles is higher than that of large particles. Compared to the result from Eq. (16), the correction for size dispersity reduces the difference between the curves for small and large particles, which is in good accordance with measurement data. Fig. 11(b) shows the results for *Case 2*. The experimental data for red and green particles are almost coincide. The prediction using Eq. (18) is, again, better than that with Eq. (16).

5.3. Mixing index

In this work, the mixing degree of particles was investigated by the improved Lacey index that was proposed by Feng et al. (2004). The index is based on the statistical analysis of variances of volume fraction of different particles in different samples, which can be given as

$$M = \frac{S_0^2 - S^2}{S_0^2 - S_r^2}, \tag{11}$$

where S^2 is the actual variance; $S_0^2 = P_s(1 - P_s)$ and $S_r^2 = P_s(1 - P_s)/N_e$, respectively, represented the variances for the completely segregated state (maximum) and the well mixed state (minimum). The variable P_s is the global volume fraction of the smallest particle in a mixture. Originally (Lacey, 1954), the index was used for mono-disperse systems. In the poly-disperse system, the concept of the equivalent number N_e is used. To keep the same total particle volume in the sample, the equivalent number N_e can be evaluated based on the number of particles in each size class and the corresponding ratio of the volume of single particle in this size class to the volume of single smallest particle. The size of the sample is fixed, while the contribution of the sample to the variance S^2 is weighted according to the equivalent number of particles. If c_i is defined as the volume fraction of the smallest particles in each

sample i and N_s is the number of samples, the variance S^2 can be expressed as

$$S^2 = \frac{1}{k_t} \sum_{i=1}^{N_s} k_{s,i} \cdot (c_i - P_s)^2, \tag{12}$$

$$k_t = \sum_{i=1}^{N_s} k_{s,i} \tag{13}$$

where $k_{s,i}$ is the weighting factor in the sample i and k_t is the total weighting factor. $k_{s,i}$ can be calculated as the ratio of the equivalent number of particles in the sample i to the maximum equivalent number of particles for all samples at each time step ($N_{e,i}/N_{e,max}$). The mixing index obtained from Eq. (11) is by definition zero for a completely segregated mixture and increases to unity for a fully random mixture.

Based on a sensitivity study, sample size was set equal to the size of the investigation region, which can satisfy the conditions that the mixing index should be close to one for the well-mixed state and close to zero for the fully segregated state. However, due to interlaced arrangements in the interface of different layers of particles, the mixing indices in the initial states of both the measurement and the simulation are slightly larger than zero in the results, as shown in Fig. 12. The maximum mixing index is lower than unity and the perfect mixing state cannot be reached under the measurement conditions.

Fig. 12(a) shows comparisons of mixing index for *Case 1* in the time period from zero to 5 s. According to the color-PTV measurement, the mixing index gradually increases from 0.15 to an equilibrium state with a mean value of approximately 0.9. The duration of the increasing stage of mixing index is approximately 1.5 s. After that, the maximum fluctuation of mixing index remains within 0.1. The simulation using Eq. (18) predicts qualitatively and quantitative comparable results with the color-PTV experiment. The inserted snapshots from color-PTV and CFD-DEM with Eq. (18) at time 2 s show the particle distributions at the corresponding mixing indices. The simulation using Eq. (16) gives relatively large deviations of both, the mean value and the fluctuations of mixing index, especially after the increasing mixedness stage. Compared with the cumulative distribution of the square root of particle
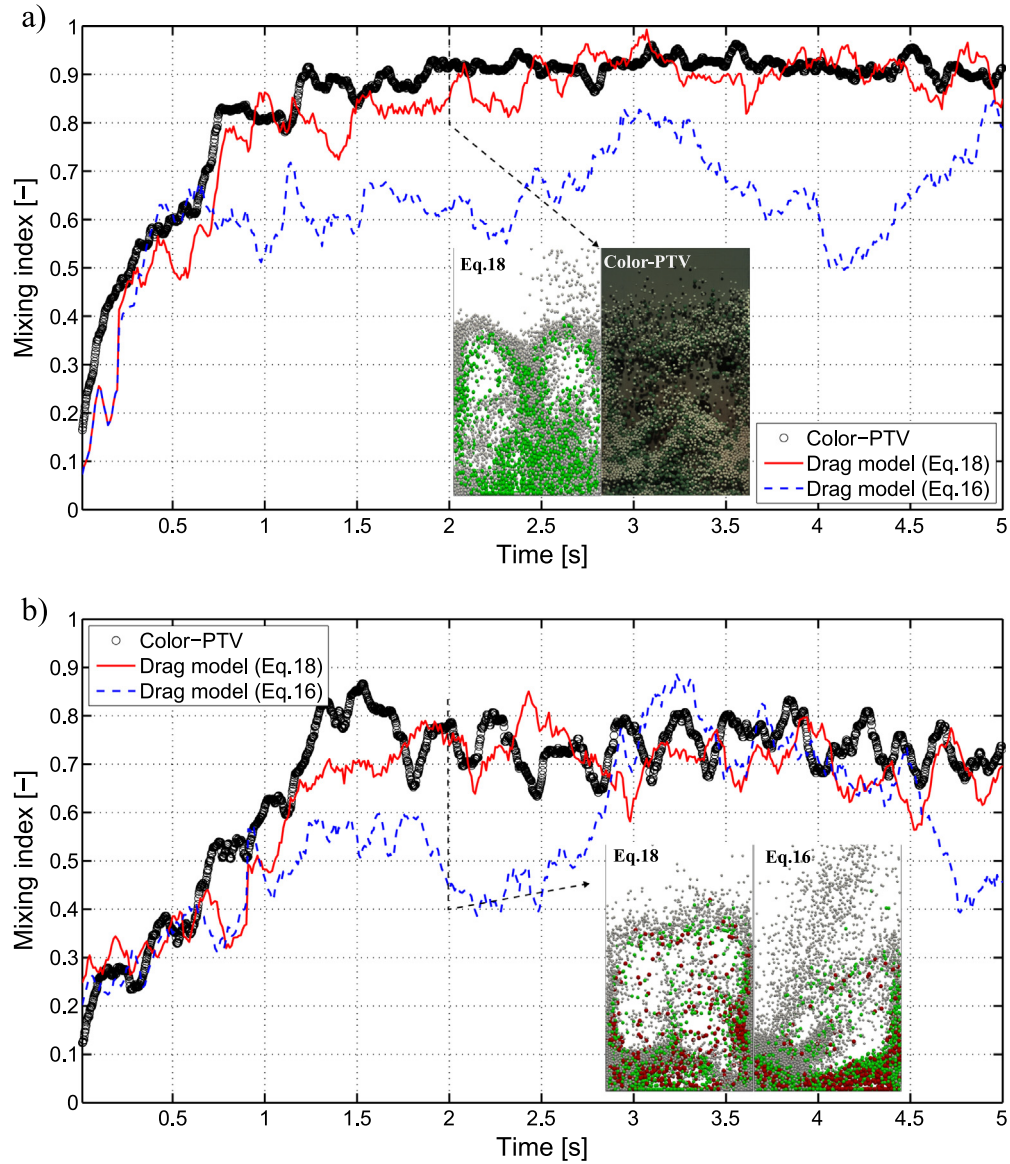
Fig. 12. Comparisons of mixing index: (a) *Case 1*, and (b) *Case 2* (snapshots at 2 s are included to visualize characteristic results of the different methods).

granular temperature (Fig. 11(a)), the large difference of particle granular temperature between small and large particles by Eq. (16) implied strong relative motions between particles of different sizes, resulting in the decrease and the fluctuation of mixing index.

For *Case 2*, red particles and green particles were considered as one component when calculating the volume fraction of white particles in the mixture. As shown in Fig. 12(b), the final mixing state for *Case 2* is much different from that of *Case 1*, although they have very similar initial bed height, Sauter mean diameter, bed mass, and the same superficial gas velocity. According to the color-PTV measurement, the mean value of mixing index after 1.5 s is approximately 0.75; and the maximum spread is larger than 0.2. The final mixing index is, thus, affected by the initial packing state. The ternary system is more difficult to be brought and kept at the relatively equilibrium than the binary system under the same fluidization conditions. The simulation using Eq. (18) still shows better performance than that based on Eq. (16). As shown in the snapshot for Eq. (16), it is difficult for small particles to enter into and stay in the void space between large particles in the corresponding CFD-DEM, leading to the under-estimation and the large fluctuation of the mixing index.

6. Conclusion and outlook

In this study, we measured the dynamics of poly-disperse particle systems in a pseudo-2D fluidized bed by a new color-PTV approach. On the basis of four quantitative criteria, the color-PTV methodology, including both particle segmentation algorithm and particle tracking algorithm, was comprehensively verified using CFD-DEM simulation data obtained for exactly the same particles and fluidization conditions. For various solid volume fractions, local particle velocities and local particle granular temperatures, the results of verification demonstrate the high accuracy and precision of color-PTV methodology in measuring velocities of individual particles with different sizes.

In the poly-disperse system, the global particle circulation in slugging flow regime can be well represented using the time-averaged volumetric particle flux. Similarly to observations in mono-disperse systems, two reversely turning but nearly symmetric vortices support the vertical and horizontal transport of particles. The change in mixing state, from the stage of increasing mixedness to quasi-equilibrium, can be quantitatively evaluated by the improved Lacey index for poly-disperse systems. The

difference in granular temperature for particles of different sizes may lead to deviations of mixing index from unity and corresponding fluctuations. The final mixing state is influenced by the initial mixture conditions, even for cases with very similar Sauter mean diameter, bed height, bed mass; and with the same superficial gas velocity.

Simulations with correction for the size dispersity effect, i.e. the over-estimation of drag force for small particles and the under-estimation of drag force for large particles, reveal better agreement with the measurements, in terms of time-averaged profiles of volumetric flux, density distributions of particle velocity, cumulative distributions of particle granular temperature and mixing index. Therefore, correction for the size dispersity effect in the drag model is essential to improve the accuracy of CFD-DEM simulation of poly-disperse particle systems in fluidized beds.

In further research, the color-PTV method will be used to retrieve the particle-scale information in specific poly-disperse particle systems, e.g. exchange rates of poly-disperse particles at over-flow weirs in horizontal fluidized beds (Bachmann et al., 2017) and mixing behavior of granules (poly-disperse and non-spherical) in rotating drums. The verification by means of CFD-DEM data can be extended to optimization of the methodology for measuring particle–particle interactions or particle–wall interactions in both uniform particle size and poly-disperse fluidized beds.

Acknowledgment

Appendix A. CFD-DEM Equations

See Tables A.1 and A.2.

Table A.1
Governing equations used in the CFD-DEM simulation for the prediction of particle-fluid flow.

Mass conservation for fluid phase (with subscript f)

$$\frac{\partial}{\partial t}(\epsilon_f \rho_f) + \nabla \cdot (\epsilon_f \rho_f \boldsymbol{u}) = 0 \tag{A.1}$$

Momentum conservation for fluid phase (model A by Zhou et al. (2010))

$$\frac{\partial}{\partial t}(\epsilon_f \rho_f \boldsymbol{u}) + \nabla \cdot (\epsilon_f \rho_f \boldsymbol{uu}) = -\epsilon_f \nabla p + \nabla \cdot (\epsilon_f \boldsymbol{\tau}_f) - \boldsymbol{F}_{pf} + \epsilon_f \rho_f \boldsymbol{g} \tag{A.2}$$

Volumetric particle-fluid interaction force in the CFD cell

$$\boldsymbol{F}_{pf} = \frac{1}{\Delta V} \sum_{j=1}^{N_1} (\boldsymbol{f}_{d,i} + \boldsymbol{f}'') \tag{A.3}$$

Newton's equations for the motion of particles

$$m_i \frac{d\boldsymbol{v}_{p,i}}{dt} = \boldsymbol{f}_{pf,i} + \sum_{i=1}^{N_2} (\boldsymbol{f}_{c,ij}^n + \boldsymbol{f}_{c,ij}^t) + m_i \boldsymbol{g} \tag{A.4}$$

$$I_{m,i} \frac{d\boldsymbol{\omega}_i}{dt} = \sum_{i=1}^{N_2} (\boldsymbol{T}_{t,ij} + \boldsymbol{T}_{r,ij}) \tag{A.5}$$

Particle-fluid interaction force on individual particle

$$\boldsymbol{f}_{pf,i} = \boldsymbol{f}_{d,i} + \boldsymbol{f}_{\nabla p,i} + \boldsymbol{f}_{\nabla \cdot \tau,i} + \boldsymbol{f}'' \tag{A.6}$$

Note that $\boldsymbol{f}''$, the sum of non-dominant particle–fluid interaction forces, is not considered in this study.

Table A.2
Equations used in the soft-sphere contact model and the particle rolling friction model.

Hertz contact forces and rolling friction torque (in Eqs. (A.4) and (A.5))

Contact force in normal direction $\boldsymbol{f}_{c,ij}^n$

$$\boldsymbol{f}_{c,ij}^n = (-k_n \delta_n - \eta_{nj} \boldsymbol{v}_{r,ij} \cdot \boldsymbol{n}) \cdot \boldsymbol{n} \tag{A.7}$$

Contact force in tangential direction $\boldsymbol{f}_{c,ij}^t$

$$\boldsymbol{f}_{c,ij}^t = \begin{cases} -k_t \delta_t - \eta_t \boldsymbol{v}_{s,ij}, & |\boldsymbol{f}_{c,ij}^t| < \mu_{fc} |\boldsymbol{f}_{c,ij}^n| \\ -\mu_{fc} |\boldsymbol{f}_{c,ij}^n| \boldsymbol{t}, & |\boldsymbol{f}_{c,ij}^t| > \mu_{fc} |\boldsymbol{f}_{c,ij}^n| \end{cases} \tag{A.8}$$

Friction torque $\boldsymbol{f}_{c,ij}^n$

$$\boldsymbol{T}_{r,ij} = -k_r k_n \delta_n \frac{\boldsymbol{\omega}_{r,ij}}{|\boldsymbol{\omega}_{r,ij}|} R_{eq} \tag{A.9}$$

Model coefficients
Normal stiffness k_n

$$k_n = \frac{4}{3} E_{eq} \sqrt{R_{eq} \delta_n} \tag{A.10}$$

Tangential stiffness k_t

$$k_t = 8 G_{eq} \sqrt{R_{eq} \delta_n} \tag{A.11}$$

Normal damping η_n

$$\eta_n = \alpha \sqrt{k_n m_{eq}} \tag{A.12}$$

Tangential damping η_t

$$\eta_t = \sqrt{\frac{2}{3}} \alpha \sqrt{k_t m_{eq}} \tag{A.13}$$

Damping ratio $\alpha(e)$

$$\alpha(e) = \begin{cases} -\sqrt{5} \ln e / \sqrt{(\ln e)^2 + \pi^2}, & e > 0 \\ -\sqrt{5}, & e = 0 \end{cases} \tag{A.14}$$

Equivalent properties
Young's modulus E_{eq}

$$E_{eq} = \left(\frac{1 - \sigma_i^2}{E_i} + \frac{1 - \sigma_j^2}{E_j} \right)^{-1} \tag{A.15}$$

Radius R_{eq}

$$R_{eq} = \left(\frac{1}{R_i} + \frac{1}{R_j} \right)^{-1} \tag{A.16}$$

Shear modulus G_{eq}

$$G_{eq} = \left(\frac{1 - \sigma_i}{G_i} + \frac{1 - \sigma_j}{G_j} \right)^{-1}, \quad G_i = \frac{E_i}{2(1 + \sigma_i)} \tag{A.17}$$

Mass m_{eq}

$$m_{eq} = \left(\frac{1}{m_i} + \frac{1}{m_j} \right)^{-1} \tag{A.18}$$

References

Ai, J., Chen, J., Rotter, J., Ooi, J., 2011. Assessment of rolling resistance models in discrete element simulations. Powder Technol. 206 (3), 269–282.

Bachmann, P., Bück, A., Tsotsas, E., 2017. Experimental investigation and correlation of the Bodenstein number in horizontal fluidized beds with internal baffles. Powder Technol. 308, 378–387.

Baek, S., Lee, S., 1996. A new two-frame particle tracking algorithm using match probability. Exp. Fluids 22 (1), 23–32.

Barrasso, D., Ramachandran, R., 2015. Multi-scale modeling of granulation processes: bi-directional coupling of PBM with DEM via collision frequencies. Chem. Eng. Res. Des. 93, 304–317.

Beetstra, R., van der Hoef, M., Kuipers, J., 2007a. Numerical study of segregation using a new drag force correlation for polydisperse systems derived from lattice-Boltzmann simulations. Chem. Eng. Sci. 62 (1–2), 246–255.

Beetstra, R., van der Hoef, M.A., Kuipers, J., 2007b. Drag force of intermediate Reynolds number flow past mono- and bidisperse arrays of spheres. AIChE J. 53 (2), 489–501.

Bokkers, G., van Sint Annaland, M., Kuipers, J., 2004. Mixing and segregation in a bidisperse gas-solid fluidised bed: a numerical and experimental study. Powder Technol. 140 (3), 176–186.

Boyce, C., Ozel, A., Rice, N., Rubinstein, G., Holland, D., Sundaresan, S., 2017. Effective particle diameters for simulating fluidization of non-spherical particles: CFD-DEM models vs. MRI measurements. AIChE J. 63 (7), 2555–2568.

Bück, A., Palis, S., Tsotsas, E., 2015. Model-based control of particle properties in fluidised bed spray granulation. Powder Technol. 270, 575–583.

Capart, H., Young, D., Zech, Y., 2002. Voronoï imaging methods for the measurement of granular flows. Exp. Fluids 32 (1), 121–135.

de Jong, J., Odu, S., van Buijtenen, M., Deen, N., van Sint Annaland, M., Kuipers, J., 2012. Development and validation of a novel Digital Image Analysis method for fluidized bed Particle Image Velocimetry. Powder Technol. 230, 193–202.

Deen, N., Van Sint Annaland, M., Van der Hoef, M., Kuipers, J., 2007. Review of discrete particle modeling of fluidized beds. Chem. Eng. Sci. 62 (1–2), 28–44.

Di Renzo, A., Di Maio, F., 2004. Comparison of contact-force models for the simulation of collisions in DEM-based granular flow codes. Chem. Eng. Sci. 59 (3), 525–541.

Feng, Y.Q., Xu, B.H., Zhang, S.J., Yu, A.B., Zulli, P., 2004. Discrete particle simulation of gas fluidization of particle mixtures. AIChE J. 50 (8), 1713–1728.

Freireich, B., Li, J., Litster, J., Wassgren, C., 2011. Incorporating particle flow information from discrete element simulations in population balance models of mixer-coaters. Chem. Eng. Sci. 66 (16), 3592–3604.

Fries, L., Antonyuk, S., Heinrich, S., Dopfer, D., Palzer, S., 2013. Collision dynamics in fluidised bed granulators: a DEM-CFD study. Chem. Eng. Sci. 86, 108–123.

Gidaspow, D., 1994. Multiphase Flow and Fluidization: Continuum and Kinetic Theory Descriptions. Academic Press, San Diego.

Goldschmidt, M., Link, J., Mellema, S., Kuipers, J., 2003a. Digital image analysis measurements of bed expansion and segregation dynamics in dense gas-fluidised beds. Powder Technol. 138 (2–3), 135–159.

Goldschmidt, M., Weijers, G., Boerefijn, R., Kuipers, J., 2003b. Discrete element modelling of fluidised bed spray granulation. Powder Technol. 138 (1), 39–45.

Goniva, C., Kloss, C., Deen, N., Kuipers, J., Pirker, S., 2012. Influence of rolling friction on single spout fluidized bed simulation. Particuology 10 (5), 582–591.

Hagemeier, T., Börner, M., Bück, A., Tsotsas, E., 2015a. A comparative study on optical techniques for the estimation of granular flow velocities. Chem. Eng. Sci. 131, 63–75.

Hagemeier, T., Roloff, C., Bück, A., Tsotsas, E., 2015b. Estimation of particle dynamics in 2-D fluidized beds using particle tracking velocimetry. Particuology 22, 39–51.

Hassan, Y., Blanchat, T., Seeley, C., 1992. PIV flow visualisation using particle tracking techniques. Meas. Sci. Technol. 3 (7), 633.

Holland, D., Müller, C., Dennis, J., Gladden, L., Sederman, A., 2008. Spatially resolved measurement of anisotropic granular temperature in gas-fluidized beds. Powder Technol. 182 (2), 171–181.

Immanuel, C., Doyle, F., 2005. Solution technique for a multi-dimensional population balance model describing granulation processes. Powder Technol. 156 (2), 213–225.

Jiang, Z., Bück, A., Tsotsas, E., 2017a. CFD-DEM study of residence time, droplet deposition, and collision velocity for a binary particle mixture in a Wurster fluidized bed coater. Dry. Technol. https://doi.org/10.1080/07373937.2017.131985.

Jiang, Z., Hagemeier, T., Bück, A., Tsotsas, E., 2017b. Experimental measurements of particle collision dynamics in a pseudo-2D gas-solid fluidized bed. Chem. Eng. Sci. 167, 297–316.

Jiang, Z., Rieck, C., Bück, A., Tsotsas, E., 2017c. Estimation of coefficient of restitution of irregularly shaped particles on horizontal substrates. In: 8th International Granulation Workshop, Sheffield (UK), Paper 18.

Joseph, G., Leboreiro, J., Hrenya, C., Stevens, A., 2007. Experimental segregation profiles in bubbling gas-fluidized beds. AIChE J. 53 (11), 2804–2813.

Kobayashi, T., Tanaka, T., Shimada, N., Kawaguchi, T., 2013. DEM-CFD analysis of fluidization behavior of Geldart Group A particles using a dynamic adhesion force model. Powder Technol. 248, 143–152.

Kuo, H., Knight, P., Parker, D., Tsuji, Y., Adams, M., Seville, J., 2002. The influence of DEM simulation parameters on the particle behaviour in a V-mixer. Chem. Eng. Sci. 57 (17), 3621–3638.

Lacey, P., 1954. Developments in the theory of particle mixing. J. Appl. Chem. 4 (5), 257–268.

Laverman, J., Roghair, I., Annaland, M., Kuipers, H., 2008. Investigation into the hydrodynamics of gas-solid fluidized beds using particle image velocimetry coupled with digital image analysis. Can. J. Chem. Eng. 86 (3), 523–535.

Lecordier, B., Demare, D., Vervisch, L.M.J., Réveillon, J., Trinité, M., 2001. Estimation of the accuracy of PIV treatments for turbulent flow studies by direct numerical simulation of multi-phase flow. Meas. Sci. Technol. 12 (9), 1382.

Link, J., Cuypers, L., Deen, N., Kuipers, J., 2005. Flow regimes in a spout-fluid bed: a combined experimental and simulation study. Chem. Eng. Sci. 60 (13), 3425–3442.

Link, J., Deen, N., Kuipers, J., Fan, X., Ingram, A., Parker, D., Wood, J., Seville, J.P.K., 2008. PEPT and discrete particle simulation study of spout-fluid bed regimes. AIChE J. 54 (5), 1189–1202.

Lu, H., He, Y., Gidaspow, D., Yang, L., Qin, Y., 2003. Size segregation of binary mixture of solids in bubbling fluidized beds. Powder Technol. 134 (1), 86–97.

Mohs, G., Gryczka, O., Heinrich, S., Mörl, L., 2009. Magnetic monitoring of a single particle in a prismatic spouted bed. Chem. Eng. Sci. 64 (23), 4811–4825.

Mörl, L., Heinrich, S., Peglow, M., 2007. Fluidized bed spray granulation. In: Salman, A., Hounslow, M., Seville, J. (Eds.), Handbook of Powder Technology, vol. 11. Elsevier, Amsterdam, pp. 21–188.

Müller, P., Seeger, M., Tomas, J., 2013. Compression and breakage behavior of $\gamma - Al_2O_3$ granules. Powder Technol. 237, 125–133.

Muzzio, F., Shinbrot, T., Glasser, B., 2002. Powder technology in the pharmaceutical industry: the need to catch up fast. Powder Technol. 124 (1–2), 1–7.

Okamoto, K., Nishio, S., Saga, T., Kobayashi, T., 2000. Standard images for particle-image velocimetry. Meas. Sci. Technol. 11 (6), 685.

Olaofe, O., Buist, K., Deen, N., van der Hoef, M., Kuipers, J., 2013. Improved digital image analysis technique for the evaluation of segregation in pseudo-2D beds. Powder Technol. 244, 61–74.

Olaofe, O., Patil, A., Deen, N., van der Hoef, M., Kuipers, J., 2014. Simulation of particle mixing and segregation in bidisperse gas fluidized beds. Chem. Eng. Sci. 108, 258–269.

Peng, Z., Doroodchi, E., Luo, C., Moghtaderi, B., 2014. Influence of void fraction calculation on fidelity of CFD-DEM simulation of gas-solid bubbling fluidized beds. AIChE J. 60 (6), 2000–2018.

Ramkrishna, D., 2000. Population Balances: Theory and Applications to Particulate Systems in Engineering. Academic Press, San Diego.

Tang, Y., Lau, Y., Deen, N., Peters, E., Kuipers, J., 2016. Direct numerical simulations and experiments of a pseudo-2D gas-fluidized bed. Chem. Eng. Sci. 143, 166–180.

Tsotsas, E., 2012. Influence of drying kinetics on particle formation: a personal perspective. Drying Technol. 30 (11–12), 1167–1175.

Tsotsas, E., 2015. Multiscale approaches to processes that combine drying with particle formation. Drying Technol. 33 (15–16), 1859–1871.

Tsotsas, E., Mujumdar, A., 2011. Modern drying technology. Product Quality and Formulation, vol. 3. WILEY-VCH Verlag GmbH & Co. KGaA, Weinheim.

Tsuji, Y., Kawaguchi, T., Tanaka, T., 1993. Discrete particle simulation of two-dimensional fluidized bed. Powder Technol. 77 (1), 79–87.

van Buijtenen, M., Börner, M., Deen, N., Heinrich, S., Antonyuk, S., Kuipers, J., 2011. An experimental study of the effect of collision properties on spout fluidized bed dynamics. Powder Technol. 206 (1–2), 139–148.

Ware, C., 2012. Information Visualization: Perception for Design. Elsevier, San Francisco.

Wen, C., Yu, Y.H., 1966. A generalized method for predicting the minimum fluidization velocity. AIChE J. 12 (3), 610–612.

Yang, S., Luo, K., Fan, J., Cen, K., 2014. Particle-scale investigation of the solid dispersion and residence properties in a 3-D spout-fluid bed. AIChE J. 60 (8), 2788–2804.

Zhou, Z., Kuang, S., Chu, K., Yu, A., 2010. Discrete particle simulation of particle-fluid flow: model formulations and their applicability. J. Fluid Mech. 661, 482–510.

Zhu, H., Zhou, Z., Yang, R., Yu, A., 2007. Discrete particle simulation of particulate systems: theoretical developments. Chem. Eng. Sci. 62 (13), 3378–3396.